ABSTRACT

RICE, ANTHONY L. Metal Organic Vapor Phase Deposition of AlN, GaN, and Their Alloys (Under the direction of Dr. Zlatko Sitar).

Chemical surface treatments were conducted on mechanically polished (MP) and chemomechanically polished (CMP) (0001)-oriented single crystalline aluminum nitride (AlN) substrates to determine a surface preparation procedure for the homoepitaxial deposition of AlN epitaxial layers by metal organic vapor phase deposition (MOCVD). MP AlN substrates characterized by atomic force microscopy exhibited 0.5 nm RMS roughness and polishing scratches, while CMP AlN substrates exhibited 0.1 nm RMS roughness and were scratch-free. X-ray photoelectron spectroscopy analysis of MP and CMP AlN substrates indicated the presence of a surface hydroxide layer composed of mixed aluminum oxide hydroxide and aluminum trihydroxide. Wet etching with sulfuric and phosphoric acid mixtures reduced the amount of surface hydroxide. Ammonia annealing at 1250 °C converted the substrate hydroxide layer to AlN and increased the RMS roughness of MP and CMP AlN substrates to 2.2 nm and 0.2 nm, respectively. AlN epitaxial layers were deposited at 1100–1250 °C under 20 Torr total pressure with a V/III ratio of 180–300 in either N2 or H2 diluent. High-resolution x-ray diffraction measurements revealed that AlN epitaxial layers deposited on MP substrates were strained due to nucleation and coalescence of AlN grains on the mechanically damaged surfaces. AlN deposited on CMP substrates was epitaxial and strain-free. Thermodynamic models for nitridation and AlN deposition were also proposed and evaluated. The surfaces of AlN epitaxial layers on misoriented AlN substrates were found to exhibit four distinct morphologies, with each morphology occupying a finite range of misorientation values. Surface pitting and misoriented grains were observed in AlN epitaxial

layers on AlN substrates. The density of these defects was non-uniform across samples with higher densities of defects in regions correspond to a low angle grain boundary in the AlN substrate. Transmission Electron Microscopy of AlN epitaxial layers showed treading dislocations at the bases of surface pits and misoriented grains. The formation of the surface pits was able to be suppressed by reduction of Al supersaturation during AlN layer deposition, consistent with capillary equilibrium theory.

$Al_xGa_{1-x}N$/GaN heterostructures ($0 \leq x \leq 1$) were deposited on (0001)-sapphire by low-pressure (20 Torr) MOCVD utilizing a range of group-III precursor and NH_3 flow rates and a deposition temperature of 1050°C. The Al-mole fraction of $Al_xGa_{1-x}N$ epitaxial layers was controlled by variations in the molar flows of triethylgallium (f_{TEG}) and trimethylaluminum (f_{TMA}). Characterization by x-ray diffraction confirmed that increasing the f_{TMA}/f_{TEG} ratio during deposition resulted in increased Al-mole fraction of $Al_xGa_{1-x}N$ epitaxial layers. A linear relationship between the experimental Al-mole fraction of $Al_xGa_{1-x}N$ epitaxial layers and the group-III precursor flows was obtained if a correction factor γ was introduced such that $x = \gamma f_{TMA} / (\gamma f_{TMA} + f_{TEG})$. This correction factor was found to be independent of group-III precursor flows but dependent on NH_3 partial pressure. The value of γ for these experiments decreased from 1.4 to 1.0 when the NH_3 partial pressure was increased from 0.8 to 16.0 Torr during $Al_xGa_{1-x}N$ deposition. The growth rate of $Al_xGa_{1-x}N$ epitaxial layers was found to be a linear combination of the independent AlN and GaN growth rates when equivalent f_{TMA} and f_{TEG} were utilized under the same deposition conditions.

Metal Organic Vapor Phase Deposition of AlN, GaN, and Their Alloys

by
Anthony L Rice

A dissertation submitted to the Graduate Faculty of
North Carolina State University
in partial fulfillment of the
requirements for the Degree of
Doctor of Philosophy

Materials Science and Engineering

Raleigh, North Carolina
2015

APPROVED BY:

_____	_____
Dr. Zlatko Sitar Committee Co-Chair	Dr. Ramón Collazo Committee Co-Chair
_____	_____
Dr. Jon-Paul Maria	Dr. Mehmet Ozturk

DEDICATION

To my friends and family,

only through your support did I overcome the most trying time of my life.

BIOGRAPHY

Anthony Rice was born on December 15, 1983 and raised in Clemons, North Carolina. He earned his BS in Materials Science and Engineering from North Carolina State University in 2006. In August of 2006, he enrolled into the doctoral program in the Materials Science and Engineering Department at North Carolina State University.

ACKNOWLEDGMENTS

I would like to thank my advisors and friends, Dr. Zlatko Sitar and Dr. Ramón Collazo, for their guidance and support through both the highs and lows of my time spent during this research. I would also like to thank my committee members Dr. Jon-Paul Maria and Dr. Mehmet Ozturk for their contributions and understanding. I would also like to acknowledge the members of the graduate school responsible for the Dissertation Completion Grant, especially Dr. Mike Carter, and their patient support over the last year that allowed me to complete this work. Special thanks to all of my co-workers who all helped me in more way than I can name: Baxter Moody, Christer-Rajiv Akouala, James Tweedie, Jinqiao Xie, Joseph Rajan, Lindsay Hussey, Marc Hoffmann, Milena Bobea, Rafi Dalmau, Ronny Kirste, Seiji Mita, and Wei Guo. Finally, I would like to thank my family for their unwavering support and for the hardships they have endured on my behalf.

TABLE OF CONTENTS

LIST OF TABLES

LIST OF FIGURES

CHAPTER 1: Introduction

1.1 Dissertation Overview

III-nitrides are a family of semiconductors composed of aluminum, gallium, and indium bonded with nitrogen. These nitrides are interesting for optoelectronic and electronic devices. They have bandgaps that make photo-detectors, LED, and lasers possible, while large breakdown fields and high electron mobilities allow for radio-frequency operation and high-power devices. AlGaN has also been shown to be a solid solution for all compositions from AlN and GaN, which allows for a range of accessible bandgaps within the same material system. The wurtzite crystal structure of the III-nitrides is non-centrosymmetric, which causes spontaneous and piezoelectric polarization. These nitrides have a relatively small lattice miss-match but with large refractive index difference between AlN and GaN allow for heterostructures such as distributed Bragg reflector. Both p-type and n-type doping to technologically useful levels has been demonstrated.

However, non-native substrates are currently the industrial standard for III-nitride devices. Relatively large lattice mismatch of these substrates with the III-nitride layers causes large dislocation densities; several types of dislocations are known to be electrically active, which limits device performance [1, 2]. Furthermore, there has been no systematic demonstration for controlling dislocation densities, as has been achieved in Si, Ge, and GaAs. One of the challenges with III-nitrides is that there is a lack of information about suitable miscuts for native substrates and about defect behavior in homoepitaxial film. There are also known issues with non-ideality with respect to the incorporation of Al and Ga into thin films with respect to the input Al and Ga concentrations during deposition. There is no

consensus among researchers as to why this non-ideality is observed or the expected degree of non-ideality for different deposition conditions [3-7]. This dissertation will address basic materials engineering challenges with the use of the native AlN substrates and develop a method for composition control in AlGaN thin films. Addressing these challenges is a prerequisite for further use of the III-nitrides with native substrates.

In the rest of this chapter, properties directly relevant to the research in this dissertation and an overview of chapters in this dissertation are described.

1.2 Nitride Properties

III-nitride semiconductor materials possess a number of interesting physical, optical, and electronic properties that allow the fabrication of novel devices. Because of their wide bandgaps and strong bond strengths, they possess physical properties superior to silicon and the conventional lower bandgap III-V compounds; these properties include: thermal conductivity, breakdown electric field, maximum electron velocity, and thermal and chemical stability. III-nitrides such as InN, GaN, and AlN typically form a hexagonal wurtzite unit cell and are partially ionic solids due to the more electronegative nitrogen anion and the less electronegative III-metal cation (In^+, Ga^+, or Al^+). Due to the largely ionic behavior of the III-N bonds, the unit cell of the III-nitrides is distorted from the ideal wurtzite unit cell and a large spontaneous polarization exists along the <0001> c-axis. As the III-metal cations have different ionic radii and bonding energies with nitrogen, the III-nitrides have different bandgap energies, lattice constants, and spontaneous polarizations. A summary of these materials parameters is summarized in Table 1-1.

Table 1-1: Properties of wurtzite InN, GaN, and AlN.

	InN	GaN	AlN
Bandgap eV]	0.7	3.4	6.1
Lattice constant: a_0 Å]	3.545	3.189	3.112
Lattice constant: c_0 Å]	5.703	5.185	4.982
Ratio c_0/a_0	1.601	1.625	1.611
Thermal conductivity W/mK]	80	230	340
Breakdown field MV/cm]		3.3	15
Electron mobility cm^2/Vs]	3200	1800	400
Spontaneous polarization As/m^2]	0.081	0.029	0.032

The non-centrosymmetric crystal structure and lack of inversion symmetry along the c-axis gives rise to two distinct polarities on the {0001} surfaces. The cation and anion atoms are arranged in bi-layers on the {0001} basal plane, the most common growth orientation for the III-nitrides, and form a pair of hexagonal close packed layers. These bi-layers define polar orientations, which are commonly referred to as the III-polarity (+*c* or (0001) orientation) or N-polarity (-*c* or (000$\underline{1}$) orientation). With respect to the III-N bond oriented along the *c*-direction, a single bond points from the III-atom to the nitrogen-atom for III-polarity, while from the nitrogen-atom to the III-atom for N-polarity, as shown in Figure 1-1.

Polar orientation should not be confused with surface termination, as each orientation may be terminated with either one of the species.

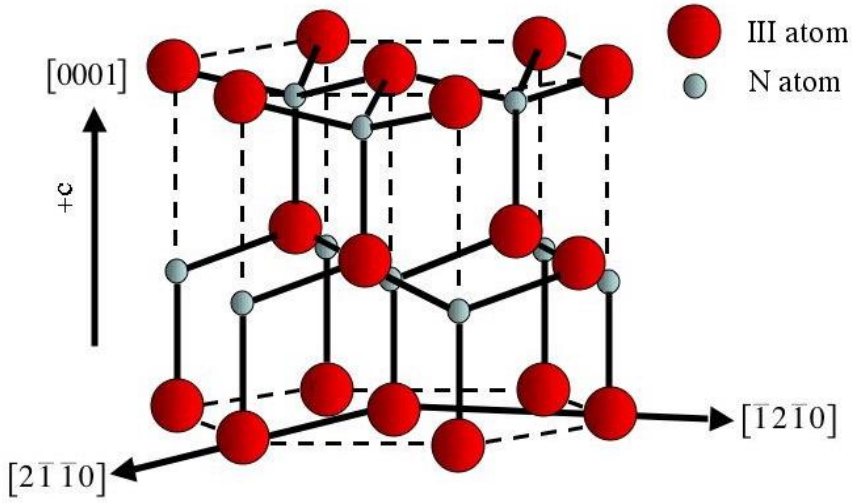

Figure 1-1: Schematic illustration of the III-nitrides' wurtzite crystal structure indicating the polarity (+*c*) along the *c*-axis.

Since most GaN-based devices are fabricated on polar {0001} surfaces, the electrical and optical properties of GaN-based heterostructures are influenced by the internal fields induced by spontaneous and piezoelectric polarizations. Therefore, performance of GaN-based devices is strongly related to the polarity of III-nitride layers. Furthermore, from the viewpoint of film growth, the quality of GaN films is influenced by polarity, since the two polarities, nitrogen (N) and gallium (Ga) polar, have different surface configurations, compositions, and chemistries. These dissimilarities can possibly lead to differences in the incorporation of impurities and the formation of defects in either Ga- or N-polar GaN. Therefore, it is very important to determine and control the polarity of GaN.

The III-nitrides form a continuous alloy system comprising ternary alloys of InGaN, InAlN and AlGaN with direct band gaps ranging from 0.7 eV for InN and 3.4 eV for GaN to 6.1 eV for AlN. They enable fabrication of optoelectronic devices emitting at wavelengths ranging from the infrared into the deep ultraviolet (UV).

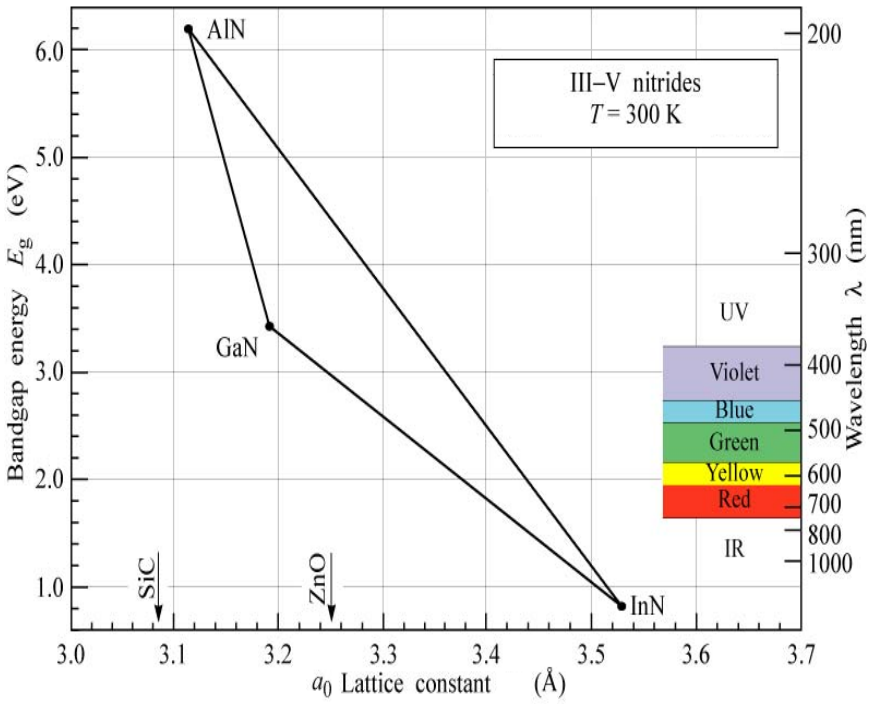

Figure 1-2: Bandgap and emission wavelength as a function of lattice parameter for III-nitride alloys.

1.3 Misorientation of Nitride Surfaces

The spontaneous formation of macro-steps is a commonly observed phenomenon during the epitaxial deposition on vicinal substrates, but the impact on device fabrication and

performance is not well understood. "If a given macroscopic surface of a crystal does not coincide in orientation with some portion of the boundary of the equilibrium shape, there will always exist a hill-and-valley structure which has a lower free energy than a flat surface" [8]. In other words, if a wafer surface is misoriented from a stable crystallographic plane by either miscut or surface curvature, macro-step formation is the result of energy minimization and is an equilibrium microstructure. Such macro-steps most commonly consist of a periodic array of alternating facets of high-symmetry planes and high Miller index planes or unreconstructed groups of atomic steps. The direction of a macro-step array is determined by the projection of the vector normal to the high-symmetry plane on the wafer surface, and the area ratio of each type of facet is fixed by the wafer miscut angle [9]. In this work, AlN macro-step formation was studied with a combination of x-ray diffraction (XRD), transmission electron microscopy (TEM), profilometry, and atomic force microscopy (AFM) techniques.

Figure 1-3 shows a schematic of the surface of a single crystal substrate with a spherically polished surface with radius of curvature, ρ. Point O represents the center of the sphere that the crystal surface lies on. Points A, B, and P form a spherical triangle on the crystal surface. Vectors OA, OB, and OP are collinear to the surface normal vector of the crystal surface at points A, B and P, respectively, and vectors OA, OB, and OP are of the same magnitude as ρ. Vector OP is also parallel to the normal of the crystallographic plane of interest and makes a logical zenith axis in a spherical coordinate system. Following the previous two statements, point P is located where the crystal surface is parallel to the crystallographic plane of interest and is the only point on such a surface that is "on-axis."

The extent and direction to which all other positions on the crystal surface are “off-axis” is defined by polar and azimuthal angles, respectively.

The polar angle α at any other point on the surface, X, is given by the angle XOP and represents the misorientation of the crystal surface from the crystallographic plane of interest. In this construction, α is zero when X=P and different from zero for any other point on the surface. For clarity, Points A and B were drawn such that α is equal for both. The azimuthal angle, χ, gives the directionality of the misorientation between the crystal surface and the crystallographic plane relative to a reference direction, i.e., a substrate flat or some conveniently chosen crystallographic direction orthogonal to the zenith axis. In this example, the angle ACB gives the difference in χ between Points A and B.

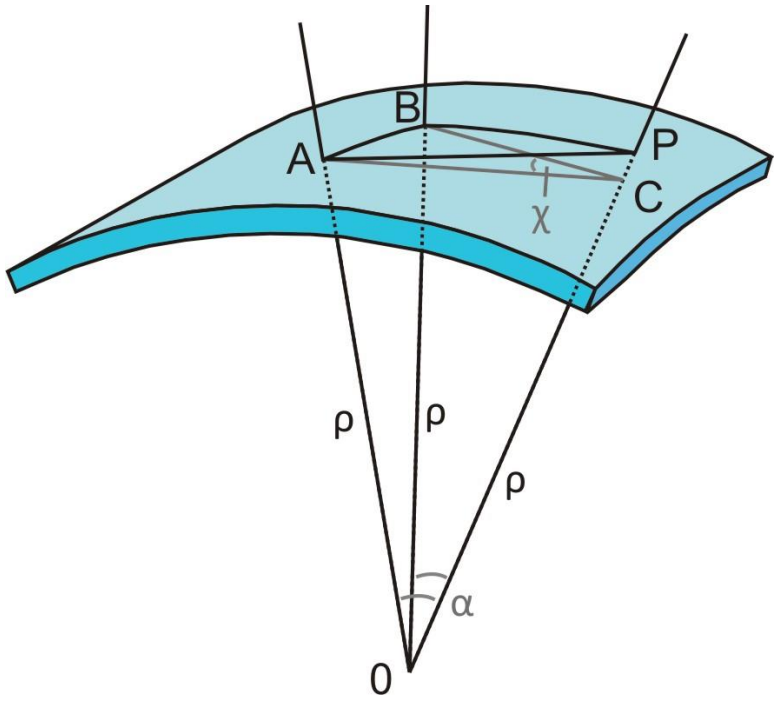

Figure 1-3: Schematic of a curved surface.

In this model, the difference in the polar angles between the two points along a great circle is given by:

$$\Delta\alpha = l/\rho, \tag{1-1}$$

where l is the length of arc between the two points. The difference in azimuthal angle between two points with the same polar angle is given by:

$$\Delta\chi = l \cdot \sin(\alpha)/\rho. \tag{1-2}$$

The angular differences between points that are not along a great circle or do not share a polar angle can be determined with Equations (1-1) and (1-2) by solving the two angular differences separately.

With the polar coordinate system and basic angular relationships described above, the variations in misorientation across a substrate surface can be characterized with a few complementary techniques. AFM topographs provide an absolute measurement of local substrate misorientation based on the separation of the periodic step structures characteristic to vicinal crystal surfaces. The precision of such misorientation measurements is limited typically by the lateral resolution, which depends on radius of the probe.

Because of this lateral resolution, there exists a maximum misorientation measureable by AFM where the periodic step features being characterized are spaced so closely together such that individual steps cannot be resolved. From the basic relationship for step spacing on a vicinal surface: $\tan(\alpha) = h/d$, where α is the misorientation between the crystal surface and a crystallographic plane, h is the step height, and d is the spacing between steps. The expected

spacing between AlN bi-layer steps of 0.25 nm height with a misorientation of ~0.4˚ would be ~36 nm. With an AFM tip radius of ~10 nm, such as those used in this study, any bi-layer step spacing less than ~40 nm would show some amount of feature convolution and would make resolving steps more closely spaced difficult if not impossible.

Profilometry measurements of surface curvature allow the change in misorientation to be determined but provide only relative measurements of misorientation across a substrate. Therefore, such measurements would ideally be combined with an absolute misorientation measurement technique such as AFM or XRD to completely characterized a substrate surface with respect to misorientation.

Point O is typically not within the wafer, given the curvatures of the wafers used in this work. Likewise, Point P may not be on the physical wafer surface when misorientation or radius of curvature is large compared to wafer diameter. The curvature is typically not constant and the substrate surfaces are often elliptical with spatially varying curvature. The curvature of portions of the wafer within ~2 mm of the substrate edge is typically an order of magnitude greater than the central region. Curvature does not provide an absolute measure of misorientation and only provides a convenient method to measure the changes in misorientation. Angle ACB is along a small circle and not a great circle, so the angular change in χ can be orders of magnitude larger than the angular change in α given the same distance between a pair of probed positions. The ratio of the change of $\Delta\chi/\Delta\alpha = 1/\sin(\alpha)$, which is large for the typically small values of α in this work.

To further examine the implication of macro-step formation on devices, TEM characterization was preformed on the epitaxial layers of an UV LED structure deposited on

an Al-polar, (0001)-oriented AlN substrate. This LED structure nominally consisted of 250 nm of homoepitaxially deposited AlN, 1 μm of n-AlGaN, quantum wells consisting of 4 pairs of 6 nm thick AlN barriers and 2 nm thick AlGaN wells, 10 nm of p-AlGaN, and 200 nm of p-GaN. The AlN substrate used in this experiment was measured to have a miscut of 4.4° with an in-plane misorientation 31.6° from a-plane using a technique detailed by Halliwell and Chua [10]. This is significant as the TEM foil was prepared with a-plane sidewalls to allow for flat cleavage surfaces, but such a cross-section is at an oblique angle to the direction of miscut and the direction of the macro-step array. To account for this, it was assumed that all angular and lateral dimensions must be corrected for a 31.6° projection using the equations:

$$\tan(a_m) = \frac{y}{x_m} \quad , \tag{1-3}$$

$$\tan(a_i) = \frac{y}{x_i} \quad , \tag{1-4}$$

$$x_i = x_m \cos(b) \quad , \tag{1-5}$$

where α_m and x_m are angular and lateral length measurements, respectively, in the TEM image plane, α_i and x_i are angular and lateral lengths, respectively, in the plane of interest, y is a vertical length measurement assumed to be parallel in both planes, and β is the angle between the TEM image plane and the plane of interest.

Figure 1-4 shows a cross sectional TEM image of this LED structure. Macro-steps can be seen at the interfaces between the top of the quantum well layers and the p-GaN layer

(Figure 1-4 (b)), between n-AlGaN layer and the bottom of the quantum well layers, and between the n-AlGaN layer and the homoepitaxial AlN layer (Figure 1-4 (c)). The contrast at the interface between the n-AlGaN layer and the bottom of the quantum well layers was too poor for quantitative analysis in large area images. It is unknown if the diffuse appearance at this interface is due to interdiffusion of aluminum and gallium or due to an artifact of TEM sample preparation and imaging. However, the quantum wells are conformal to the n-AlGaN layer such that the macro-steps seen in the quantum wells are likely a direct continuation of the underlying n-AlGaN layer macro-steps, and, as the quantum wells are thin, both the top and bottom quantum well interfaces are likely reproductions of the n-AlGaN macro-steps. The angle of each macro-step relative to (0001)-AlN can be determined by measuring the angle between a ray drawn from the macro-step minimum on the (0001)-facet of the macro-

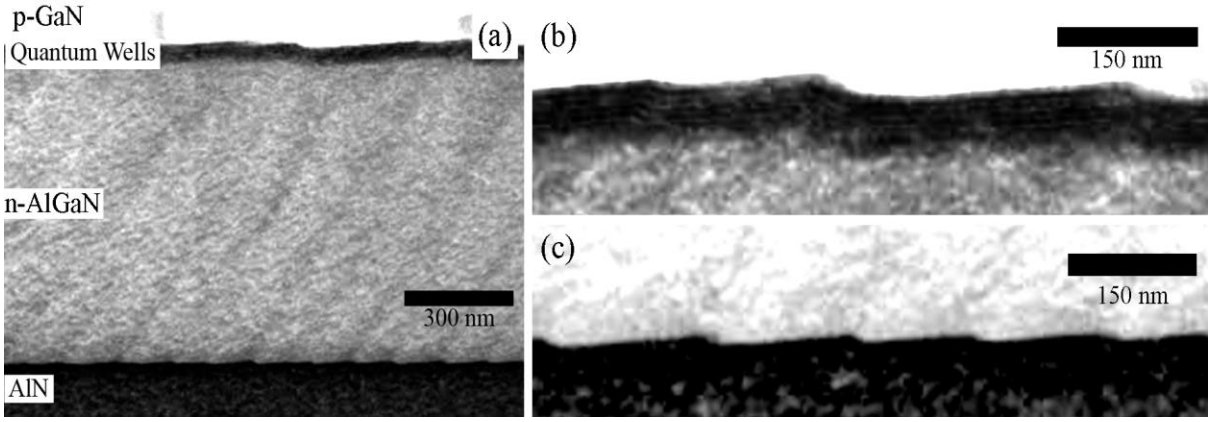

Figure 1-4: (a) Cross-sectional TEM images of the UV LED structure and magnifications of the (b) quantum well interfaces and (c) AlN and n-AlGaN interface. Macro-steps can be observed at all interfaces. Streak-like features can be observed in the n-AlGaN layer. Each streak-like feature terminates at a macro-step at the AlN or quantum interfaces.

step to the apex of the macro-step and the ray drawn from the macro-step minimum on the (0001)-facet to the macro-step minimum on the opposing high index or unreconstructed facet. A schematic for the angle measurement procedure can be seen in Figure 1-5.

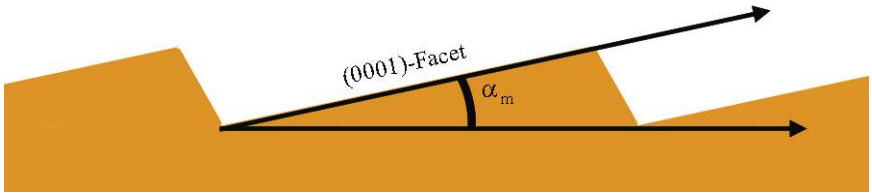

Figure 1-5: Schematic representation of a macro-step cross-section and the angular measurement in the TEM image plane, α_m.

The angle of the macro-steps in the TEM cross-section was measured to be 4.2° ± 1.2° for the homoepitaxial AlN and 4.0° ± 2.8° for the n-AlGaN. Both measured macro-step angles are in good agreement with the XRD measured value of miscut. While similar angular values at both interfaces were expected, as both interfaces must conserve the same macroscopic misorientation with the same ratio of (0001)-facet area to high index or unreconstructed facet area, the size of individual macro-steps can vary between materials due to the differences in surface energy and intrinsic surface stress. The macro-step period of the AlN layer was measured to be 100 nm ± 24 nm and the period of the n-AlGaN layer was found to be 199 nm ± 59 nm. The macro-step height of the AlN layer was found to be 7 nm ± 2 nm and the height of the n-AlGaN layer was found to be 14 nm ± 4 nm. The AlN macro-step period and height are consistent with AFM measurements taken of homoepitaxial AlN layers deposited on AlN substrates with similar miscut.

A direct consequence of macro-step formation is a periodic array of discontinuities that may interfere with the deposition of thin layers such as those utilized in quantum well structures. In the worst case, wetting behavior of the materials at a faceted interface may prevent uniform deposition, and, for such a case, the minimum thickness of each layer in a quantum well structure should exceed the height of surface macro-steps. AFM characterization of thin GaN layers deposited on homoepitaxial AlN layer with macro-steps suggests such a case. Figure 1-6 shows AFM images of GaN layers of 2.5 nm and 5 nm nominal thicknesses deposited on homoepitaxial AlN layers with macro-step heights of approximately 3 nm. From these images, it can be seen that GaN deposits preferentially at the apex of macro-steps and that gaps in the GaN coverage remain even after 5 nm of GaN deposition.

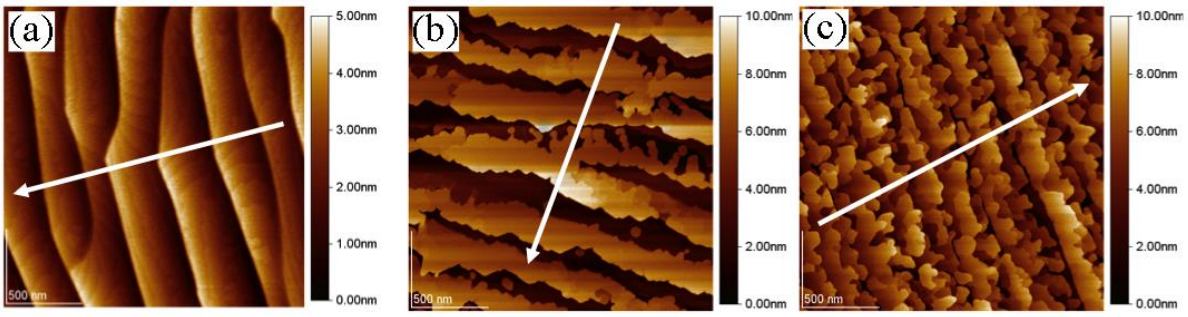

Figure 1-6: 2x2 μm^2 AFM images of (a) bare AlN, (b) following nominally 2.5 nm of GaN deposition, (c) following nominal 5 nm of GaN deposition. All image were taken of samples grown on AlN substrates with miscuts of ~1.5°. The directions of the macro-step arrays are indicated by the white arrow in each image.

However, AlGaN layers are expected to provide better wetting due to greater supersaturation and greater driving force for nucleation. Additionally, the wetting behavior is also expected to improve when reducing the composition difference between each layer as the interfacial energy between the layers and the strain from lattice mismatch is reduced. Figure 1-7 shows the quantum well of the UV LED structure near a macro-step. Both the AlN barriers and AlGaN wells are conformal to the underlying n-AlGaN layer, but the layer thicknesses are increased by ~10% near the macro-step. Approximately 15% of the total quantum well area is affected by measureable thickness variation due to the macro-steps.

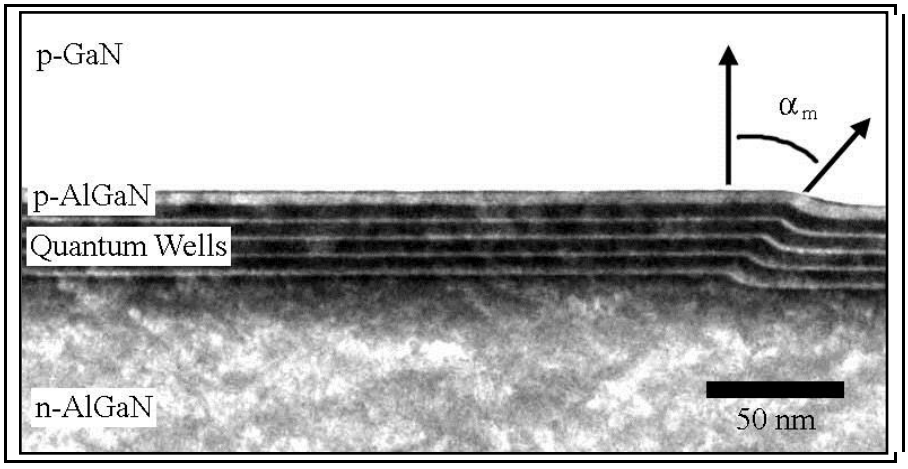

Figure 1-7: Cross-sectional TEM image of the quantum wells near a macro-step with the angular measurement in the TEM image plane for macro-step advancement, α_m.

While the ramifications of such thickness fluctuations have not yet been characterized on this structure, photoluminescence measurements of AlGaAs and GaAs quantum well structures deposited on vicinal GaAs substrates, with locally thicker quantum wells near macro-steps, show a reduction of the peak emission energy and a broadening of the emission

peak relative to an identical quantum well structure deposited on a nominally on-axis GaAs substrates [11].

The angle of macro-step advancement was also determined to be 36.2° using the quantum well structure (see Figure 1-7). This angle is similar to the angle of the streak features, 34.7°, seen in the n-AlGaN layer (Figure 1-4). Additionally, each streak-like feature terminates at a macro-step at the AlN interface, suggesting that the streaks are related to the advancement of the macro-steps. The nature of the contrast mechanism responsible for the streak features is due to compositional fluctuations.

1.4 Overview of Dissertation

Chapter 2 covers studies of homoepitaxial deposition of AlN thin films by metalorganic chemical vapor deposition on single crystalline AlN substrates. These experiments cover surface studies to determine the morphology and chemistry of as-received AlN substrates utilizing XPS and AFM, respectively, and the development of a pre-deposition chemical treatment to prepare the wafer for further processing. Due to reactivity of AlN with ambient atmosphere, a native aluminum hydroxide is expected; therefore, a thermodynamic treatment of the nitridation of Al_2O_3 (as α-sapphire) by ammonia at high temperature is presented as a possible surface treatment during substrate preparation. A derivation to calculate the supersaturation of aluminum vapor at the vapor-solid interface is shown. Deposited homoepitaxial AlN thin films are characterized by XRD, AFM, and TEM to probe the suitability of the pre-deposition chemical treatment and to examine defect

behavior, particularly focusing on defects that are related to the inherited properties of the substrates such as threading dislocations and miscut.

The third chapter addresses the development of a model of composition control during the deposition of AlGaN thin films by MOCVD for the full compositional range from AlN to GaN. This was conducted by depositing AlGaN thin films using a range of mixtures of Al, Ga, and N precursors (trimethylaluminum, triethylgalium, and ammonium, respectively). AlGaN thin films were characterized by XRD to determine composition. A linear relationship between the experimental Al-mole fraction of $Al_xGa_{1-x}N$ layers and the group-III precursor molar flows was observed such that:

$$x = \delta * f_{TMA} / (\delta * f_{TMA}) + f_{TEG}), \quad (1\text{-}6)$$

where δ is a correction factor independent of group-III precursor flows but dependent on other deposition parameters. δ for these experiments was found to decrease when the NH_3 partial pressure was increased during AlGaN film deposition.

Chapter 4 concludes this dissertation by providing a summary of the research findings and suggested directions for future research.

1.5 References

1 A. Armstrong, A. R. Arehart, B. Moran, S. P. Den Baars, U. K. Mishra, J. S. Speck, and S. A. Ringel, Appl. Phys. Lett. **84**, 374 (2004).

2 D. G. Zhao, H. Yang, J. J. Zhu, D. S. Jiang, Z. S. Liu, S. M. Zhang, Y. T. Wang, and J. W. Liang, Appl. Phys. Lett. **89**, 112106 (2006).

3 S. Bass, C. Pickering, M. Young, J. Cryst. Growth **64**, 68 (1983).

4 C. Kuo, J. Yuan, R. Cohen, J. Dunn, and G. Stringfellow, Appl. Phys. Lett. **44**, 550 (1984).

5 D. Mazzarese, A. Tripathi, W. Conner, K. Jones, L. Caleron, and D. Eckart, J. Electron. Mater. **18**, 369 (1989).

6 A. Thon and T.F. Kuech, Appl. Phys. Lett. **69**, 55 (1996).

7 L.V. Interrante, L.E. Carpenter II, C. Whitmarsh, W. Lee, M. Garbauskas, and G.A. Slack, Mater. Res. Soc. Proc. **73**, 359 (1986).

8 C. Herring, Physical Review, **82** 87 (1951).

9 E. D. Williams, R. J. Phaneuf, J. Wei, N. C. Bartelt, and T. L. Einstein, Surface Science, **294** 219 (1993).

10 M. A. G. Halliwell and S. J. Chua, Journal of Crystal Growth, **192** 456 (1998).

11 T. Fukui, J. Ishizaki, S. Hara, J. Motohisa, and H. Hasegawa, Journal of Crystal Growth, **146** 183 (1995).

CHAPTER 2: AlN Homoepitaxy

2.1 Overview

Single crystalline aluminum nitride (AlN) is a promising substrate material for AlN and aluminum gallium nitride (AlGaN) based electronic and optoelectronic devices, due to similar thermal expansion coefficients and relatively small lattice mismatches. However, the reactivity of AlN with moist air and water at ambient conditions necessitates a comprehensive understanding of surface preparation techniques if optimal epitaxy is to be achieved on AlN substrates [1-8].

A number of studies on powder, thin film, and bulk AlN have shown that AlN forms an aluminum hydroxide layer when exposed to moist air [1, 3-5, 7, 8] or to water [2, 4, 6, 8]. This hydroxide layer appears to form rapidly after initial exposure, but then stabilizes and inhibits further oxidation [1, 8]. The thickness of this hydroxide layer has been reported to be 5-10 nm for AlN single crystals following one day of exposure to ambient air [1] and ~1 nm for (0001)-oriented AlN epitaxial layers after several weeks of exposure [8]. The hydroxide layer reportedly consists of aluminum oxide hydroxide (AlOOH) [8] or a mixture of AlOOH and aluminum trihydroxide ($Al(OH_3)$) [2, 3, 6, 7].

Sapphire is a common substrate material for III-nitride deposition by metalorganic chemical vapor deposition (MOCVD), and the behavior of sapphire during surface treatments prior to heteroepitaxy is expected to be similar to the behavior of the hydroxide layer on AlN substrates due to the similar chemistries and reactivity [9-18]. Sapphire surface treatment schemes typically include both *ex situ* and *in situ* processes to achieve suitably terminated surfaces. *Ex situ* surface treatments involve the removal of surface contamination with

solvents and acids. *In situ* sapphire surface treatments include sapphire nitridation by exposure to ammonia at high temperatures [9-12, 14, 17, 18] or to nitrogen plasma [13, 15, 16] to convert several nanometers of sapphire to epitaxial AlN [10, 14, 16]. It is expected that the aluminum hydroxide species native to AlN surfaces can likewise be transformed to AlN.

Once the AlN substrate surface is suitably prepared, homoepitaxial deposition of AlN can be achieved. MOCVD is a common commercial technique for III-nitride deposition due to large throughputs and film uniformity. MOCVD of AlN involves many variables: temperature, pressure, V/III ratio, diluent gas, and the input partial pressure of precursors species. Koukitu *et al.* have proposed a thermodynamic supersaturation model that encompasses all such deposition parameters and allows the epitaxial layer behavior to be predicted [19, 20]. In particular, the behavior of a growing crystal surface strongly depends on supersaturation, according to the Burton–Cabrera–Frank (BCF) model of crystal growth, critical nuclei size and the rate of nucleation are expected to vary with supersaturation [21].

In this chapter, the effects of wet etching and high temperature ammonia annealing on the AlN substrates surfaces is evaluated. A thermodynamic model for the nitridation of sapphire is proposed and implemented to find suitable conditions depending on the available processing capabilities. In addition, a thermodynamic AlN supersaturation model is used to analyze the behavior of AlN deposition on (0001)-oriented AlN substrates with up to 2° of misorientation.

2.2 Experimental Procedure

AlN substrates used in this study were processed from AlN boules grown by physical vapor transport and were nominally (0001)-oriented with less than 2° of misorientation and possessed convex lenticular surfaces with a radius of curvature greater than 1 m. Further details of the AlN boule growth can be found elsewhere [22-24]. All substrates used in this study were mechanically polished (MP), and a number of the substrates were then chemo-mechanically polished (CMP). MP substrates were lapped and fine polished with abrasives of decreasing size, resulting in a smooth optical finish that exhibited no features in differential interference contrast (DIC) microscopy. However, remnant polishing scratches were observed by AFM, similar to published results for AlN bulk crystals (e.g., Figure 3 in reference 25). CMP substrates were subjected to additional polishing in a proprietary alkaline slurry of sub-micron sized abrasives following the mechanical polishing procedure.

Prior to epitaxy, as-polished substrates were ultrasonically cleaned sequentially in acetone, methanol, and then deionized water for 5 minutes each. Following cleaning, the substrates were wet etched in a 3:1 sulfuric : phosphoric acid mixture for 10 minutes at 90°C. Wet etched substrates were then rinsed in deionized water for 15 minutes, dried with flowing nitrogen, and transferred into a vertical, cold-walled, rf-heated, low-pressure MOCVD reactor. The reactor was then pumped to high vacuum (less than 10^{-6} Torr) and back filled with ammonia. Substrates were annealed in flowing ammonia (Blue Ammonia, Solkatronics Chemicals, Morrisville, PA) at 60 Torr for 15 minutes at 1250°C, as measured by an optical pryometer on the substrate holder. The temperature ramp-time from room temperature to 1250°C was less than 5 minutes. AlN epitaxial layers were then deposited by MOCVD

utilizing trimethylaluminum (TMA) and ammonia as the aluminum and nitrogen precursors, respectively. AlN epitaxial layers of 1 μm thickness were deposited at 1100–1250°C under 20 Torr total pressure with a V/III ratio of 180–300 in either N_2 or H_2 diluent.

AlN substrate surface chemistry was assessed by x-ray photoelectron spectroscopy (XPS) utilizing a VG Instruments hemispherical analyzer with Al Kα radiation in an analysis chamber with 1×10^{-10} Torr base pressure. Core level spectra were collected with 20 eV pass energy. The spectrometer work function was calibrated to 84.0 eV with the Au $4f_{7/2}$ photoelectron line of a standard sample. All reported binding energies include a correction for sample charging determined by the binding energy shift of the adventitious C 1*s* line from 284.6 eV. All spectra were fitted with Voigt profiles, and the deconvolution of each core level spectra was constrained such that each spectral component included the same Gaussian and Lorentzian contributions. Elemental peak areas were converted to compositions using the atomic sensitivity factor for x-ray sources at 90° [26]. The peak areas of Al 2*p*, C 1*s*, N 1*s*, and O 1*s* core level spectra were used to determine the surface molar ratios of elements. Surface morphology was characterized by atomic force microscopy (AFM) using a DI Dimension-3000 and a JEOL JSPM-5200 in tapping mode. Crystalline quality of AlN substrates and epitaxial layers were characterized by high-resolution x-ray diffraction (HRXRD), which was performed using a Philips X'Pert materials research diffractometer with a Cu K_α x-ray source in a triple-axis configuration with a four-bounce Ge 220 crystal monochromator on the incident beam side and a three-bounce Ge analyzer crystal. X-ray characterization was also utilized to determine the misorientation between the substrate surface and the (0001) crystallographic plane using the previously mentioned diffractometer

in a double-axis configuration with an open detector and the procedure described by Halliwell and Chua [27]. Surface curvature of AlN substrates was characterized by profilometry utilizing a Veeco Dektak 150 surface profilometer.

AlN substrate surfaces were characterized in the as-polished condition and following the wet etching, ammonia annealing, and epitaxial deposition procedures. As-polished substrates were typically stored in ambient air for several weeks prior to characterization or processing. Substrate exposure to ambient air following wet etching or ammonia annealing was limited to a few minutes prior to loading substrates into the XPS vacuum analysis chamber. AFM image acquisition was completed within 24 hours following ammonia annealing or epitaxial deposition.

2.3 *Ex situ* Processes

Figure 2-1 shows 2 μm × 2 μm AFM images of MP and CMP substrates with and without bi-layer steps. MP substrates had numerous polishing scratches, while CMP substrates were featureless or showed only bi-layer steps; RMS roughness was found to be 0.5 nm and 0.1 nm, respectively. The observation of bi-layer steps or the lack thereof on CMP substrates is thought to be the result of differences in substrate misorientation as bi-layer steps have only been observed for CMP substrates with less than ~0.4˚ misorientation from (0001). From the basic relationship for step spacing on a vicinal surface: $\tan(\alpha) = h/d$, where α is the misorientation between the crystal surface and a crystallographic plane, h is the step height, and d is the spacing between steps, the expected spacing between AlN bi-layer steps of 0.25 nm height with a misorientation of ~0.4˚ would be ~36 nm. With an AFM

tip radius of ~10 nm, such as those used in this study, any bi-layer step spacing less than ~40 nm would show some amount of feature convolution and would make resolving steps more closely spaced difficult if not impossible. These results suggested that work-damage introduced during mechanical polishing was successfully reduced by chemo-mechanical polishing.

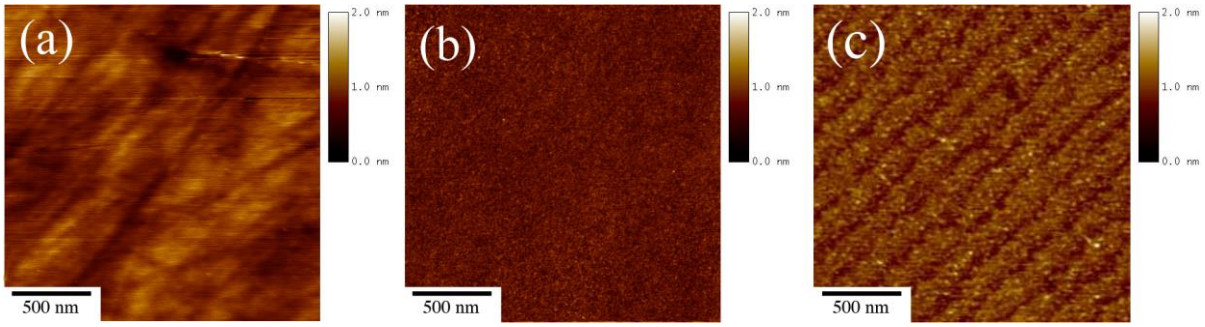

Figure 2-1: 2 μm × 2 μm AFM images of a polished AlN substrates surfaces. No bi-layer steps are visible for (a) MP and (b) CMP substrates with misorientations greater than ~0.4° while bi-layers are visible for (c) CMP substrate with misorientations less that ~0.4°.

XPS analysis of MP and CMP substrates indicated the presence of a layer of mixed hydrated alumina species. The amount of surface contamination by carbon and oxygen was greater for MP substrates than for CMP substrates: the Al:N:O:C surface molar ratios were found to be 40:32:16:12 and 46:37:9:8, respectively. Figure 2-2 shows a summary of surface molar ratios following the various surface treatments. A representative high resolution O 1*s* core level peak for a MP substrate is shown in Figure 2-3. The broad O 1*s* core level peak was deconvoluted into three components with binding energies of 530.4 eV, 531.6 eV, and 532.8 eV. The O 1*s* core level peaks of CMP substrates were also deconvoluted into three

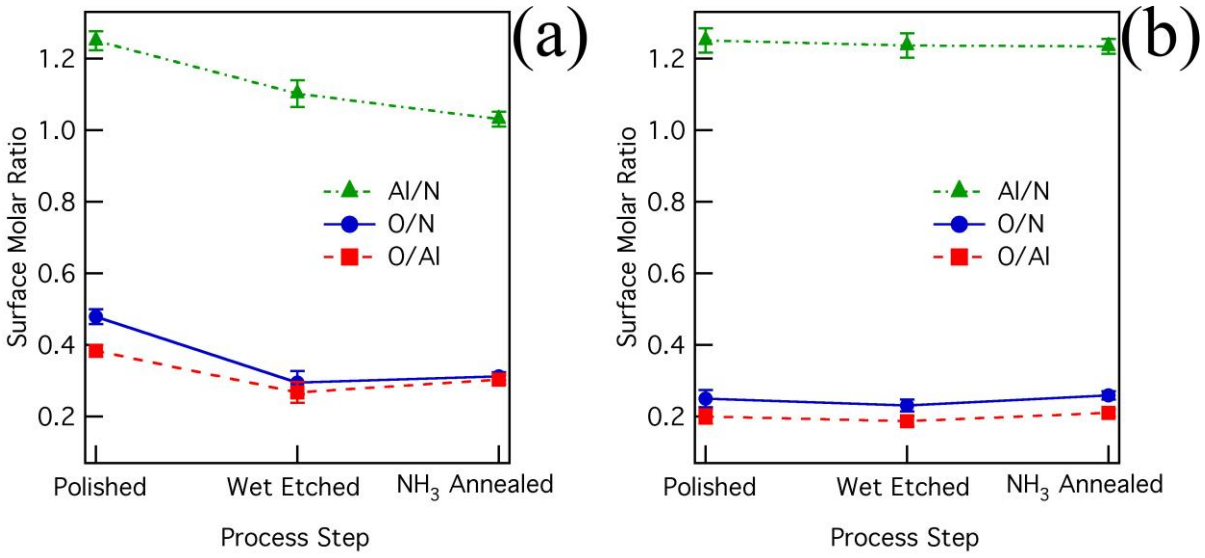

Figure 2-2: Surface molar ratios of (a) MP and (b) CMP AlN substrates following each surface preparation process.

components with binding energies of 530.7 eV, 531.7 eV, and 533.2 eV. In a previous XPS study of hydrated aluminas, Tsuchida and Takahashi deconvoluted the O 1*s* spectra into two components attributed to O^{2-} and OH^- species with binding energies ranging from 530.7 eV to 531.5 eV and from 532.0 eV to 532.3 eV, respectively [28]. This assignment scheme was found to be consistent in works with AlN epitaxial layers deposited on SiC [5] and sapphire [8]. However, it appears that a detectable amount of physisorbed or intercalated water was present for as-polished substrates in the current study. The O 1*s* core level binding energy for H_2O has been reported to be 533.1 eV [29]. From these results, the O 1*s* core level components with the lowest, intermediate, and greatest binding energies were assigned as O^{2-}, OH^-, and H_2O, respectively. The O 1*s* core level component molar ratios O^{2-}:OH^-:H_2O were H_2O, respectively. The O 1*s* core level component molar ratios O^{2-}:OH^-:H_2O were found to

be 20:60:20 and 36:52:12 for the MP and CMP substrates, respectively. A summary of the O 1*s* core level component molar ratios following the various surface preparation processes can be seen in Figure 2-4. The observation of a detectable H_2O peak component is likely the result of prolonged exposure to water and abrasion during polishing, as both the surface molar ratio of oxygen and the component molar ratio of H_2O are increased for the MP substrates relative to the less damaged CMP substrates.

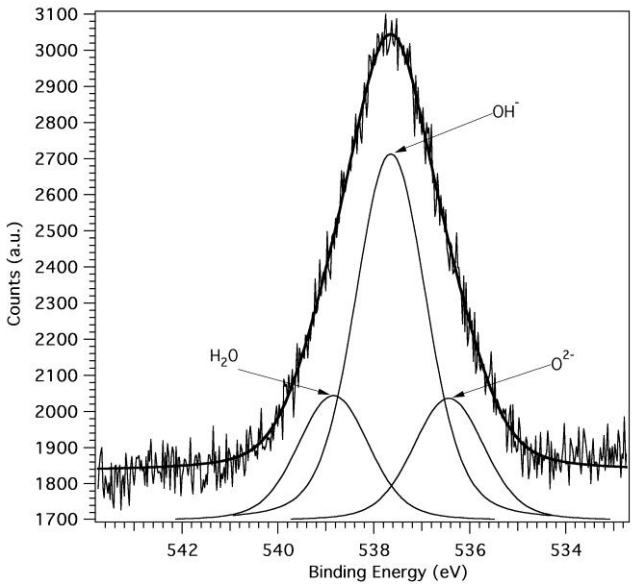

Figure 2-3: Deconvoluted O 1*s* core level peak of a MP AlN substrate surface

Wet etching of as-polished substrates resulted in a reduction of oxygen and carbon surface contamination. The Al:N:O:C surface molar ratios were found to be 44:40:12:4 and 48:39:9:4 for wet etched MP and CMP substrates, respectively. Additionally, the wet etching modified the O 1*s* core level component molar ratios of O^{2-}:OH^-:H_2O to 20:70:10 and 38:50:12 for the MP and CMP substrates, respectively. Wet etching in the 3:1 sulfuric :

phosphoric acid mixture at 90°C for durations greater than 10 minutes had no additional effect on the amount or composition of the hydroxide layer, implying an equilibrium or steady state between the hydroxide layer and acid mixture. Wet etching at temperatures greater than 130°C modified the O 1*s* core level component molar ratios of O^{2-}:OH^-:H_2O to approximately 0:80:20 but did not further reduce the total amount of surface hydroxide. Wet etching at temperatures greater than 180°C began preferential etching of scratches on MP substrates and formed both symmetric and asymmetric hexagonal pits, on MP and CMP substrates, presumably decorating dislocations.

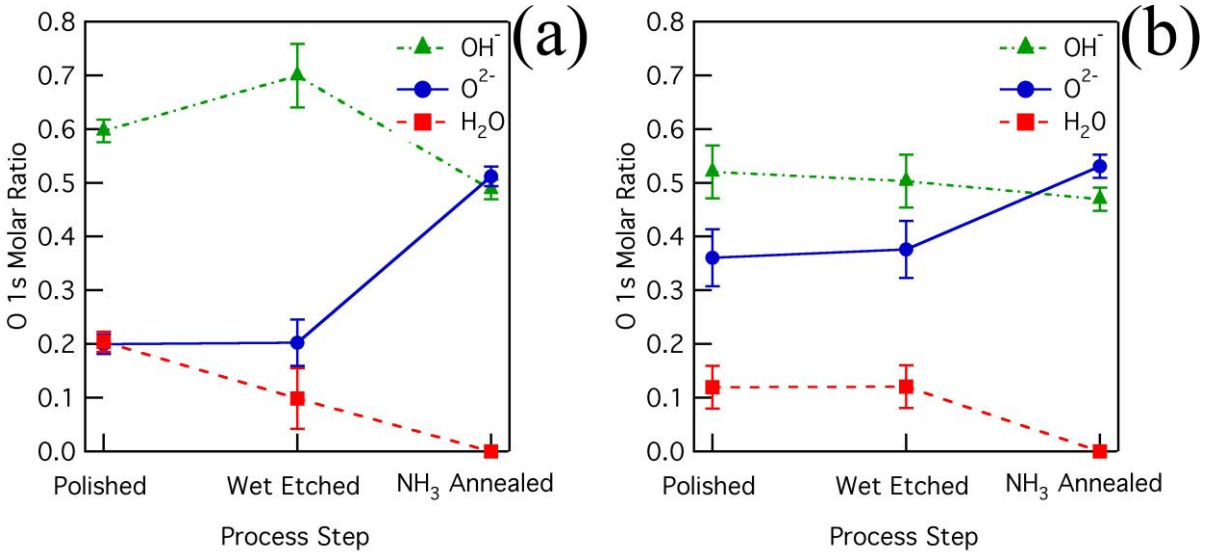

Figure 2-4: O 1*s* core level peak component molar ratios of (a) MP and (b) CMP AlN substrates following each surface preparation process.

2.4 Ammonia Anneal

The reactions considered during high temperature nitridation of AlN substrates surfaces were:

$$Al_2O_3(s) + 2NH_3 \longleftrightarrow 2AlN(s) + 3H_2O \tag{2-1}$$

and

$$2NH_3 \rightarrow N_2 + 3H_2. \tag{2-2}$$

The nitridation of sapphire by ammonia, Equation 2-1, was chosen in favor of reactions involving the aluminum hydroxide species because sapphire is expected to be the most stable oxidized state above 477°C and represents the least energetically favorable transformation [30]. The equilibrium constants for the nitridation and dissociation reactions can be defined as

$$K_1 = \frac{a_{AlN}^2 P_{H_2O}^3}{a_{Al_2O_3} P_{NH_3}^2} \tag{2-3}$$

and

$$K_2 = \frac{P_{N_2} P_{H_2}^3}{P_{NH_3}^2}, \tag{2-4}$$

respectively, where a_{AlN}, $a_{Al_2O_3}$, P_{H_2O}, P_{NH_3}, P_{N_2}, and P_{H_2} are the activities of AlN and sapphire and the equilibrium partial pressures of water, ammonia, nitrogen, and hydrogen,

respectively. To solve this system of equations, constant total pressure, P_T, and the input molar ratio of hydrogen and nitrogen, γ, were assumed to be

$$P_T = P_{H_2O} + P_{NH_3} + P_{N_2} + P_{H_2} \tag{2-5}$$

and

$$g = \frac{3P_{NH_3} + 2P_{H_2} + 2P_{H_2O}}{P_{NH_3} + 2P_{N_2} + [AlN]}. \tag{2-6}$$

If the molar quantity of AlN were not taken into account, the system would be undetermined. Assuming P_{H_2O} can be neglected, as it is expected that P_{H_2O} is much smaller than the other equilibrium partial pressures, Equation 2-5 becomes:

$$P_T = P_{NH_3} + P_{N_2} + P_{H_2}. \tag{2-7}$$

With the additional assumption that the molar quantity of AlN involved in the reaction is negligibly small compared to the molar quantities of the gaseous species, Equation 2-6 becomes:

$$g = \frac{3P_{NH_3} + 2P_{H_2}}{P_{NH_3} + 2P_{N_2}}. \tag{2-8}$$

If ammonia is the only input gas, $\gamma = 3$ and $P_{N_2} = \frac{1}{3}P_{H_2}$. Substitution into Equation 2-7 gives $P_{H_2} = \frac{3}{4}\left(P_T - P_{NH_3}\right)$ and substitution into Equation 2-4 gives:

$$\frac{27}{256}\left(P_T - P_{NH_3}\right)^4 - K_2 P_{NH_3}^2 = 0. \qquad (2\text{-}9)$$

The solution of Equation (2-9) gives P_{NH_3}. Substitution of P_{NH_3} into Equation (2-3) allows P_{H_2O} to be determined. Figure 2-5 shows P_{H_2O} as a function of temperature for P_T of 20, 60, and 100 Torr with ammonia as the only input gas. The difference between P_{H_2O} and the actual experimental water partial pressure of the system determines the driving force for nitridation and is expected to increase with temperature for a given experimental water partial pressure. Following this statement, Figure 2-5 can be viewed as a phase diagram for nitridation with respect to the actual water partial pressure of the system: the region under the curve corresponds to nitriding conditions and the region above the curve corresponds to

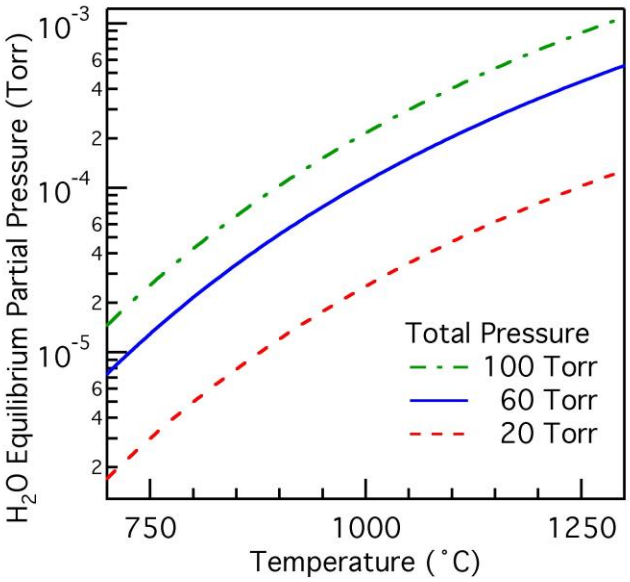

Figure 2-5: Equilibrium partial pressure of water in flowing ammonia at 20, 60, and 100 Torr total pressure.

oxidizing conditions. It should be noted that this analysis is limited to only the driving force of the overall process. No kinetic analysis or conclusions are intended, as additional processes may hinder nitridation. Indeed, studies suggest that the diffusion of reactants in the solid is the rate limiting process for nitridation of sapphire by ammonia [14, 16, 17]. The ammonia anneal utilized in this study, 1250°C at 60 Torr with ammonia as the only input gas, is expected to provide nitriding conditions for partial pressures of water less than 5×10^{-4} Torr. The background partial pressure of water in the MOCVD reactor was determined to be approximately 1×10^{-5} Torr based on reactor base pressure and water contamination of the ammonia, well below the necessary partial pressure of water for nitridation.

Figure 2-6 shows 2×2 μm^2 AFM images of MP and CMP substrates following ammonia annealing. The RMS roughness of ammonia annealed MP and CMP substrates was found to be 2.2 nm and 0.2 nm, respectively. Ammonia annealed MP substrates had protrusions of 100 nm average width and 3.5 nm average height. Protrusions of similar dimensions have been reported for sapphire surfaces nitrided by ammonia annealing [12, 18] and nitrogen plasmas [13, 16]. It is likely that the CMP substrates were roughened to a lesser extent due to the reduced amount of surface hydroxide compared to the MP substrates.

The surface molar ratio Al:N:O:C following ammonia annealing was found to be 42:40:13:5 and 47:38:10:5 for the MP and CMP substrates, respectively. The O 1*s* core level component molar ratio O^{2-}:OH^-:H_2O was found to be 51:49:0 and 53:47:0 for the MP and CMP substrates, respectively. It is thought that this amount and composition of surface hydroxide is indicative of the initial oxidation of an (0001)-oriented AlN surface upon exposure to moist air. Additionally, an O/N and O/Al surface molar ratio of ~ 0.2 may represent the

method detection limit of oxygen for any experimental procedure including entailing the exposure of AlN to moist air or water. The nearly 1:1 O^{2-}:OH^- ratio following ammonia annealing suggests that the hydroxide layer is overwhelmingly comprised of stoichiometric AlOOH; however, the thermodynamic stability of hydrated alumina species predicts that the formation of $Al(OH)_3$ to be more energetically favorable at ambient conditions 29]. The observation of AlOOH may be due to intermediate steps of oxidation 7 or kinetic barriers to oxidation of (0001)-oriented AlN surfaces [8], as $Al(OH)_3$ has been observed in the oxidation of polycrystalline and powdered AlN [2, 3, 7].

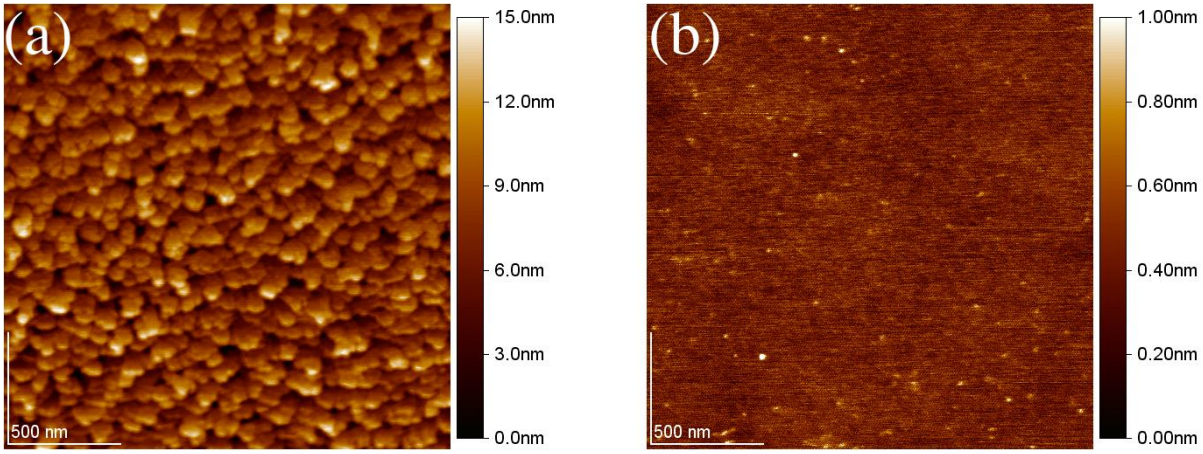

Figure 2-6: 2 μm × 2 μm AFM images of (a) MP and (b) CMP AlN substrates following ammonia annealing at 1250°C.

2.5 Deposition of AlN

The deposition of AlN epitaxial layers by MOCVD is a nonequilibrium process driven by the supersaturation of aluminum in the gas phase. The driving force for deposition

of AlN is determined for a system by the deviation from thermodynamic equilibrium. The change in free energy of the reaction can be quantified by $\Delta G = -RT \ln(\sigma_{Al} + 1)$, where the supersaturation of aluminum, σ_{Al}, is the normalized difference between the input partial pressure of aluminum, P_{Al}^{o}, and the equilibrium partial pressure of aluminum, P_{Al}:

$$s_{Al} = \frac{P_{Al}^{o} - P_{Al}}{P_{Al}}. \tag{2-10}$$

It is assumed that P_{Al}^{o} is equal to the input partial pressure of TMA, as TMA pyrolysis is not expected to be a rate limiting reaction at typical AlN deposition temperatures. P_{Al} can be evaluated with a simplified chemical reaction:

$$Al(g) + NH_3 \leftrightarrow AlN(s) + \frac{3}{2} H_2(g) \tag{2-11}$$

with an equilibrium constant

$$K_{AlN} = \frac{a_{AlN} P_{H_2}^{3/2}}{P_{Al} P_{NH_3}}, \tag{2-12}$$

where $P_{H_2}^{o}$ and $P_{NH_3}^{o}$ are the input partial pressures of hydrogen and ammonia and $\log_{10}K = -14.2 + (3.17\times10^{4}/T) + 2.33\log_{10}T$, where T is the absolute temperature [19, 20, 31]. Figure 2-7 shows theoretical curves of σ_{Al} as a function of V/III ratio and temperature generated by the methodology previously described by Mita *et al.* [30], replacing Equation (2-10) in that work with:

$$P_r = P_{Al}^f \left(1 + \frac{V}{III}^f\right)\left(1 - F^f\right) + P_T F^f, \tag{2-13}$$

where

$$P_{Al}^f \equiv \frac{P_T f_{Al}^i}{f_T^i + \alpha f_{NH_3}^i},$$

$$\frac{V}{III}^f \equiv (1-\alpha)\frac{V}{III}^i,$$

$$F^f \equiv \frac{f_{H_2}^i + \frac{3}{2}\alpha f_{NH_3}^i}{f_{H_2}^i + f_{IG}^i + 2\alpha f_{NH_3}^i}, \text{ and}$$

$$f_T^i \equiv f_{Al}^i + f_{NH_3}^i + f_{H_2}^i + f_{IG}^i,$$

where f_{Al}^i, $f_{NH_3}^i$, $f_{H_2}^i$, and f_{IG}^i are the input flows of group III species, group V species, H_2, and inert gas, respectively. This replacement takes into account the change in total molar flow of gas entering and exiting the system due to the decomposition of NH_3. σ_{Al} values for all theoretical curves were calculated using 20 Torr total pressure and P_{Al}^o = 3.5 mTorr. Temperature was fixed at 1250°C while V/III was fixed at 200 for curves in Figures 2-7(a) and 2-7(b), respectively. Important trends illustrated in Figure 2-7 include: σ_{Al} is greater with nitrogen diluent than with hydrogen diluent, σ_{Al} increases with increasing V/III ratio with a greater rate of increase at low V/III ratios than at large V/III ratio, and σ_{Al} decreases exponentially with increasing temperature.

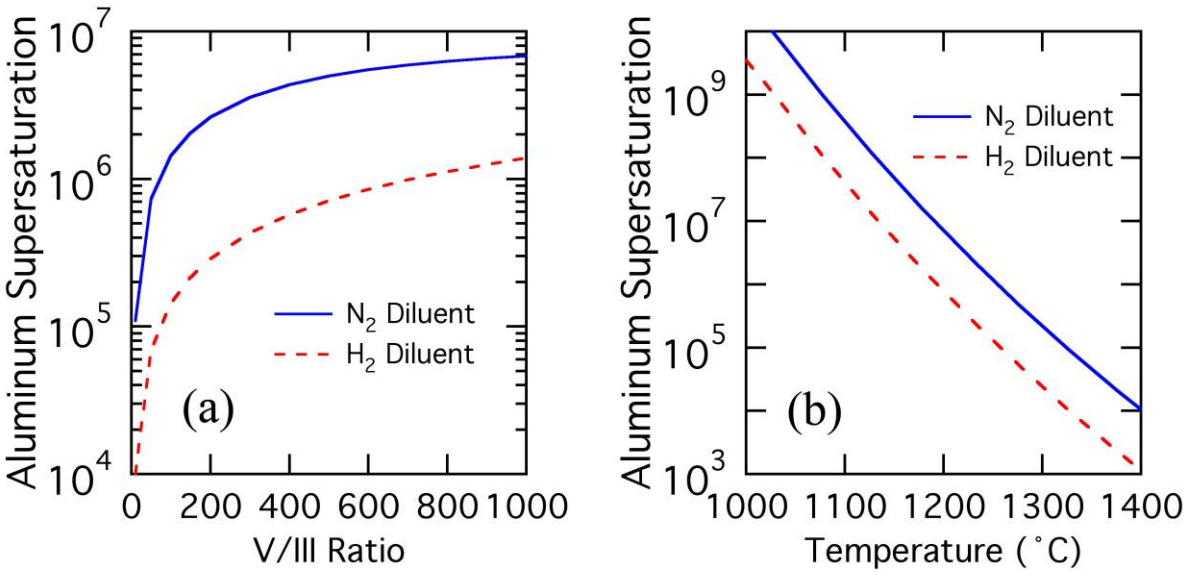

Figure 2-7: Aluminum supersaturation as a function of (a) V/III ratio and (b) temperature. Aluminum supersaturation values were determined with (a) temperature of 1250°C and (b) V/III of 200.

Figure 2-8 shows DIC microscope images of AlN epitaxial layers deposited on MP and CMP substrates. Deposition on MP substrates resulted in the decoration of macroscopic defects, such as scratches (inset of Figure 2-8 (a)), while deposition on CMP substrates yielded featureless surfaces, as seen in Figures 2-8 (a) and (b), respectively.

Figure 2-9 shows HRXRD measurements of the (0002) AlN 2θ-ω peak of epitaxial layers deposited on MP substrates with σ_{Al} of 2.2×10^6, 2.2×10^5, and 7.0×10^4. The shoulders exhibited in the HRXRD scans, which probed the AlN lattice parameter along the 0001 direction, indicated that epitaxial layers deposited on MP substrates were strained, suggesting nucleation and coalescence of AlN grains on the mechanically damaged and roughened surfaces.

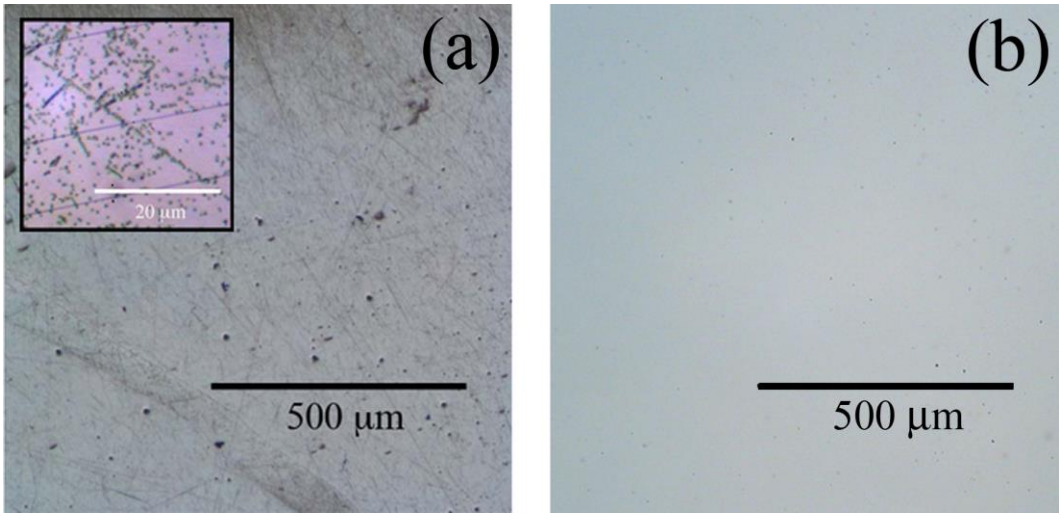

Figure 2-8: DIC micrographs of AlN epitaxial layers deposited on (a) MP and (b) CMP AlN substrates. The inset of Figure (a) shows decoration of scratches.

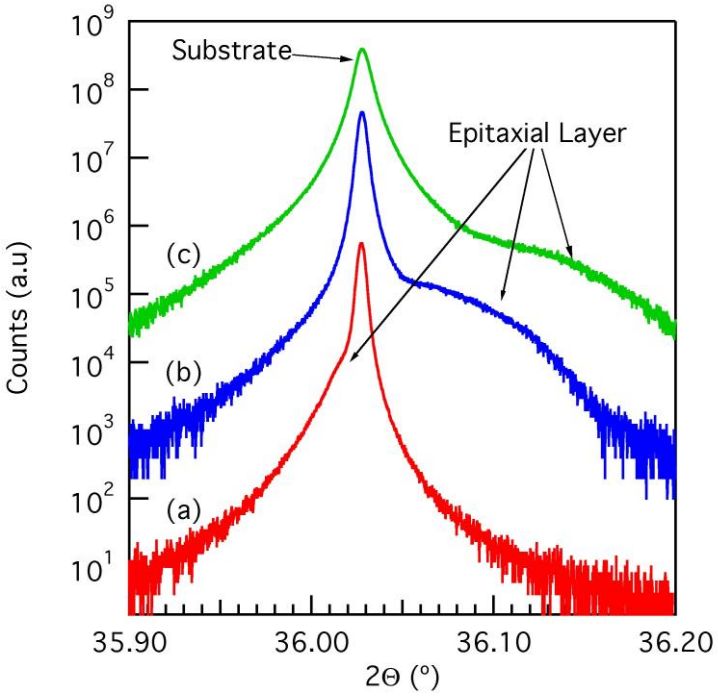

Figure 2-9: HRXRD 2θ-ω scans of (0002) AlN for AlN epitaxial layers deposited with aluminum supersaturation of (a) 2.2×10^{6}, (b) 2.2×10^{5}, and (c) 7.0×10^{4} on MP AlN substrates.

According to the BCF model of crystal growth [21], the critical diameter D of a two dimensional nucleus has the following dependence on supersaturation:

$$\frac{1}{D} \mu \ln(\sigma_{Al} + 1). \tag{14}$$

From here, the strain state of the AlN epitaxial layer would be expected to vary with σ_{Al} if AlN nuclei were formed. It was found that the in-plane strain was compressive for epitaxial layers deposited at σ_{Al} of 2.2×10^6 and became increasing tensile for decreasing σ_{Al}. Considering the three main sources of strain in epitaxial thin films – lattice mismatch, thermal mismatch, and island coalescence – and assuming that the lattice and thermal mismatches were negligible due to homoepitaxial deposition, then the observed strain is attributable to the coalescence of AlN grains nucleated on the MP substrate surfaces. Figure 2-10 shows HRXRD measurements of the (0002) AlN 2θ-ω peaks of a CMP substrate before and after epitaxial deposition and indicates that the film was epitaxial and strain-free. The full-width at half-maximum intensity of ω-rocking curve scans of the (0002) reflection of the CMP substrates before and after epitaxial layer deposition was unchanged at 25 arcsec, indicating the high crystalline quality of AlN substrates and homoepitaxial layers. These observations suggest that the surfaces of CMP substrates were free of mechanical damage and that the chemical surface treatments employed resulted in a suitable film/substrate interface.

Figure 2-11 shows AFM characterization of AlN epitaxial layers deposited on MP and CMP substrates which exhibited a combination of bi-layer micro-steps of ~2.5 Å height

and bunched macro-steps of 1-10 nm height. Figure 11(a) shows a pair of micro-cracks (indicated by arrows) in an AlN epitaxial layer deposited on a MP substrate with σ_{Al} of 7.0×10^{4}. This micro-cracking is consistent with the tensile in-plane strain observed by HRXRD for epitaxial layers deposited on MP substrates with the lower σ_{Al} utilized in this study. Figure 2-11(b) shows protrusions of ~1 nm in height with an area density of $\sim10^{9}$ cm^{-2} on an epitaxial layer deposited on a CMP substrate. These protrusions are thought to be related to surface oxidation, as the size and area density of the protrusions increased with increasing duration of exposure to moist air at ambient conditions.

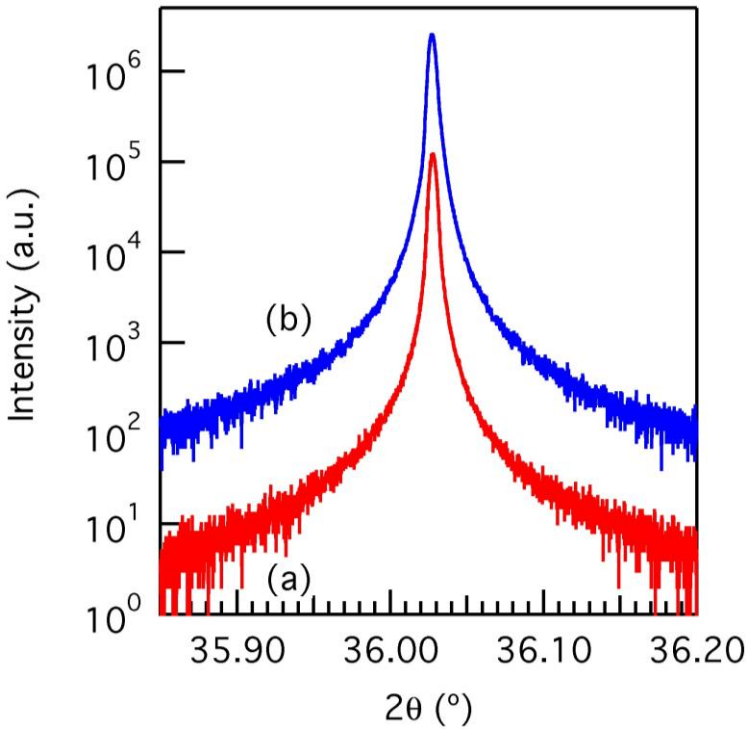

Figure 2-10: HRXRD 2θ-ω scans of (0002) AlN for a CMP substrate (a) before and (b) after AlN epitaxial deposition.

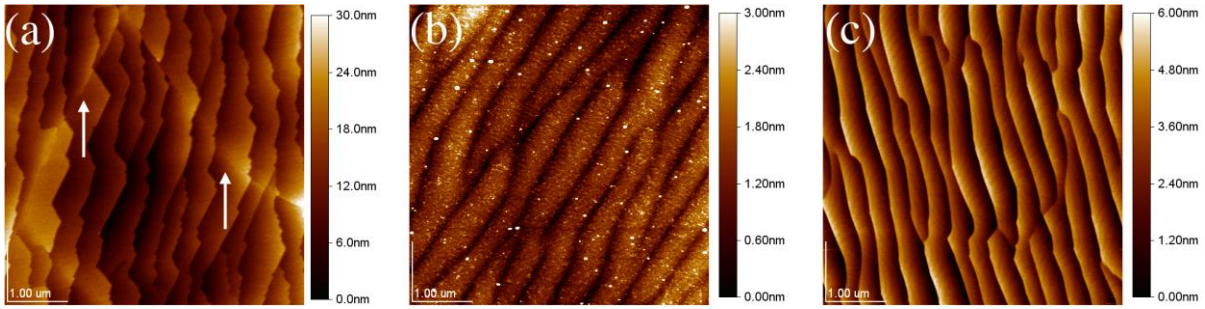

Figure 2-11: 5 μm × 5 μm AFM images of AlN epitaxial layers deposited on (a) MP and (b) (c) CMP substrates. σ_{Al} during epitaxial layer deposition was (a) 7.0×10^{4}, (b) 1.4×10^{7}, and (c) 4.2×10^{4}. The arrows in Figure (a) indicate a pair of micro-cracks.

2.6 Effects of Substrate Misorientation

The previous sections of this chapter demonstrated the sample preparation necessary for homoepitaxial deposition of AlN. The remainder of this chapter will describes the effects of substrate misorientation and deposition conditions on AlN films that are both homoepitaxial and strain free. One particularly noteworthy property of the AlN substrates used in this study was that the lenticular shape of the substrate surfaces, which offered a continuum of misorientations between the surface of the crystal and the (0001) crystallographic plane.

To determine the variation of misorientation across a single AlN substrate, numerous AFM topographies were taken on individual substrates. The results of one such AFM study are presented in Figure 2-12, which shows the relative positions where AFM topographies were collected on a single as-CMPed AlN substrate in addition to the approximate

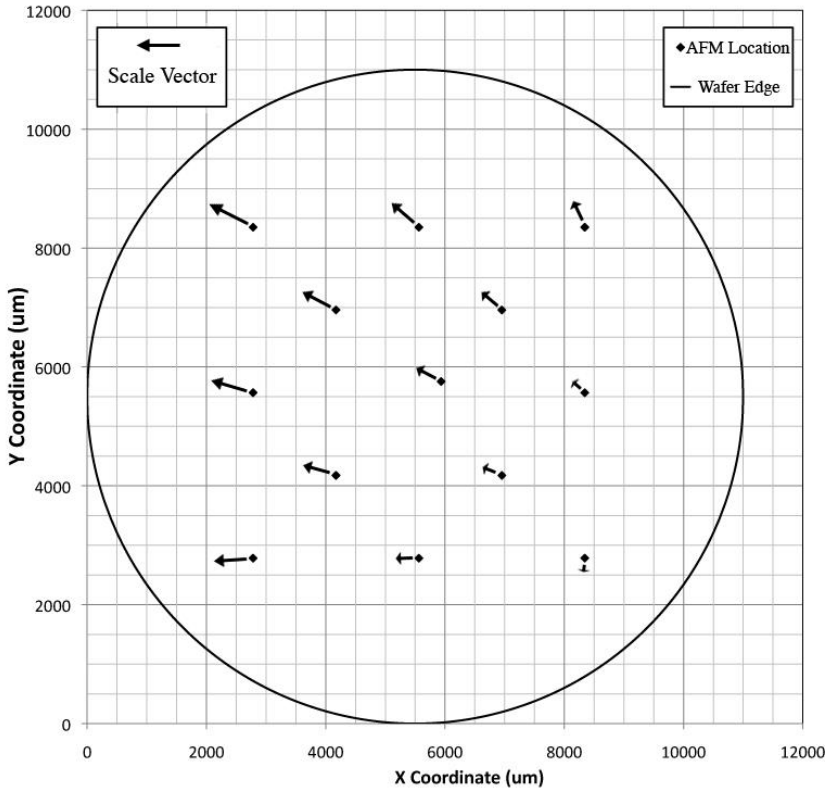

Figure 2-12: Vector field representation of misorientation as a function of position on a lenticular AlN substrate surface. Vectors signify both the magnitude and direction of misorientation as a projection of a unit vector normal to the substrate surface at each position onto the (0001) crystallographic plane oriented parallel to the image plane. The scale vector represents the projection of the unit vector at 0.3° from <0001> onto (0001).

boundaries of the AlN substrate on which they were collected. Figure 2-12 is oriented such that the (0001) crystallographic plane is parallel to the viewing plane and the scale vector represents the projection of a unit vector of arbitrary magnitude oriented 0.3° from the <0001> crystallographic direction onto the (0001) crystallographic plane. Immediately next to each position that an AFM topograph was collected is a vector showing the projection onto

the (0001) crystallographic plane of a unit vector of the same arbitrary magnitude but normal to the substrate surface at the position the AFM topograph was collected. The magnitude of the projected vector for each AFM position corresponds to the degree of misorientation determined using the relationship for step spacing on a vicinal surface, $\tan(\alpha) = h/d$, and the mean step height and width observed in the AFM topograph. The direction of the vector for each AFM position corresponds to the direction of the surface normal vector that is oriented perpendicular to the individual step features in the step array. The AFM study illustrated in Figure 2-12 showed a range of misorientations between 0.05° to 0.30° and showed directions of misorientation that form an arc of 148°. Repeating these procedures on additional AlN substrates suggests that 0.2° to 0.4° of variation in misorientation was typical for the surfaces of AlN substrates used in this study, when only regions more than 2 mm from the substrate edges are considered. The inclusion of regions near the substrate edge results in variations in misorientation as large as 5° with the direction of misorientation typically making a full circle.

Figure 2-13 shows AFM topographies of AlN homoepitaxial films deposited with a σ_{Al} of 4.2×10^4 in regions with misorientation ranging from 0.03° to 0.75° with each image being representative of one of the four major categories of surface morphologies observed under these deposition condition: (a) step flow, (b) step bunching, (c) a transitional morphology, and (d) layer-by-layer. Figure 2-14 shows the (a) average step width and (b) average step height as functions of substrate misorientation for AlN deposited with a σ_{Al} of 4.2×10^4 in regions with misorientation up to 1.22°. The discontinuity in step behavior that occurs at ~0.2° has been marked to indicate the transition from misorientation values which show only

features of bi-layer height to misorientation values which also exhibit step features of larger heights.

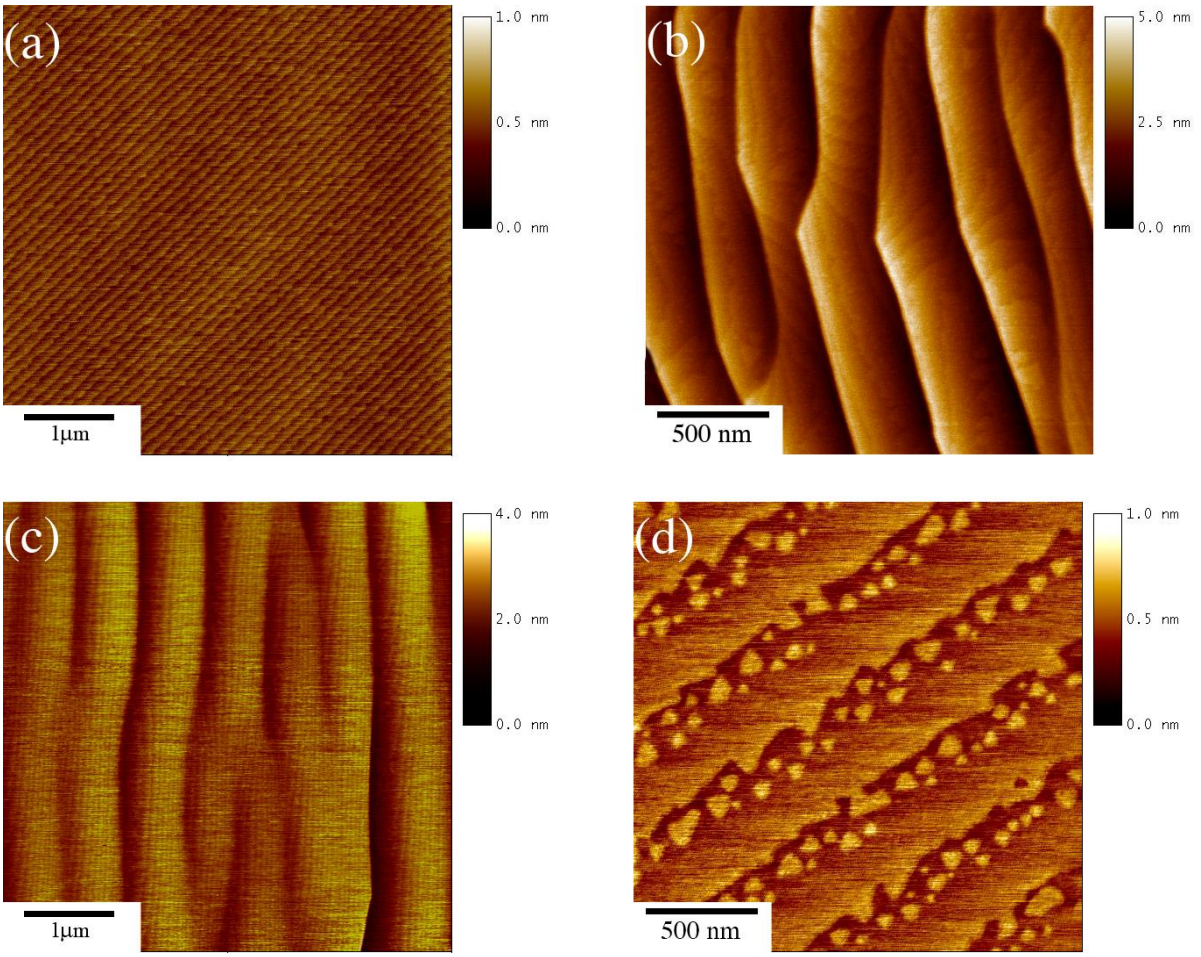

Figure 2-13: AFM topography of AlN homoepitaxial films deposited with a σ_{Al} of 4.2×10^4 in regions with misorientation ranging from 0.03° to 0.75°. Representative images of (a) step flow, (b) step bunching, (c) transitional, and (d) layer-by-layer morphologies are show.

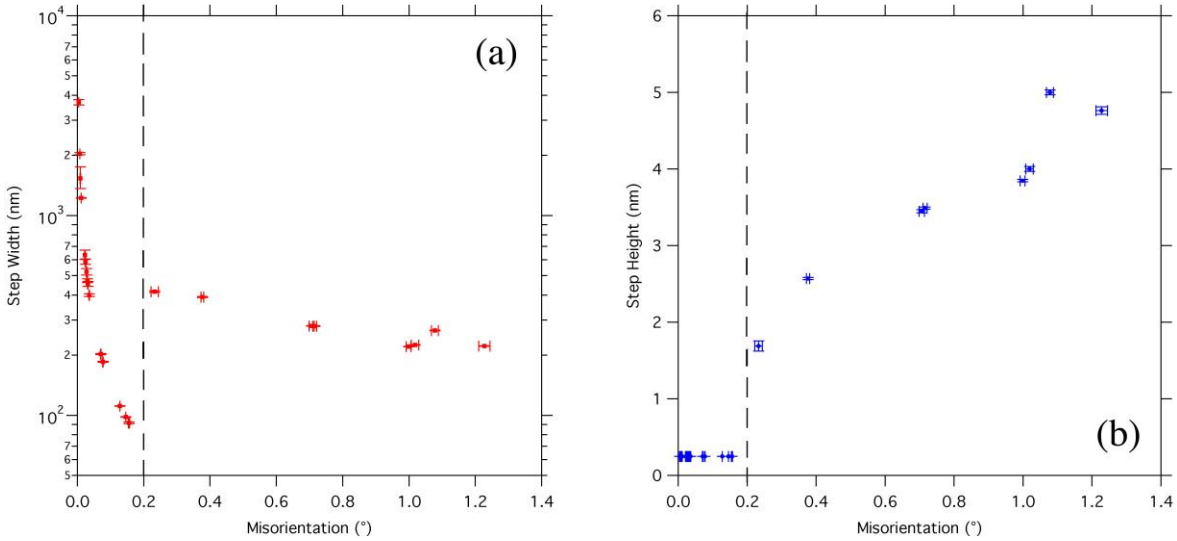

Figure 2-14: (a) Step width and (b) step height as a function of substrate misorientation for AlN homoepitaxial films deposited with a σ_{Al} of 4.2×10^4. The dashed, vertical line at 0.2° indicates the crossover from misorientations exhibiting step features of only bi-layer height to misorientations that are dominated by step features of much larger heights.

The step flow morphology was characterized by periodic arrays of bi-layer steps. The spacing of such steps was found to be a function of the misorientation of the substrate surface with the (0001) crystallographic plane, while the orientation of the step array was found to be collinear with the orientation of the projection of the surface normal vector on the (0001) crystallographic plane. The step flow morphology was observed in regions with misorientation values between 0.07° and 0.2°. The spacing between bi-layer steps was found to be between 70 nm and 200 nm in regions exhibited the step flow morphology. The RMS roughness in regions exhibiting step flow morphology was found to be ~0.1 nm in 5 μm × 5 μm scan areas.

The step bunching morphology was characterized by a periodic array of alternating high-symmetry (0001)-oriented crystal facets and high Miller index crystal facets or un-reconstructed clusters of bi-layer steps with a distinct, cusp-like edges present at the interface between such facets. Un-clustered bi-layers were present on the (0001)-oriented facets but did not exhibit the periodic spacing of the bi-layer steps arrays in the step flow morphology. The step bunching morphology was observed in regions with greater than 0.2° misorientation. As with the step flow morphology, the orientation of the periodic array coincided with the orientation of the projection of the surface normal vector on the (0001) crystallographic plane. The orientation of the bi-layer steps on (0001)-oriented facets had no dependence on the orientation of the surface normal vector beyond being pinned at the boundaries of the facet that they occupied. Both the height and spacing of the facet arrays were found to be a function of misorientation of the crystal surface with (0001) crystallographic plane. The periodic spacing between (0001)-oriented facets was found to be between 250 nm and 400 nm, and the step height between (0001)-oriented facets was found to be between 1.5 nm and 5.6 nm for AlN films deposited on substrates with less than 2° misorientation. The RMS roughness in regions exhibiting the step bunching morphology varied from 0.3 nm to 5.8 nm for 5 μm × 5 μm scan areas. The differences in step heights between regions with different misorientations contributed significantly to the observed range of RMS roughness values, and RMS roughness increasing monotonically with increasing step heights. For scan areas confined to individual (0001)-oriented facets, RMS roughness values varied from 0.2 nm to 0.4 nm which indicates that the morphology on the

(0001)-oriented facets is relatively uniform compared to the overall morphology in the step bunching regions.

The transitional morphology was characterized by wave-like features without the cusp-like edges of facets characteristic to the step bunching morphology and by bi-layer steps without a uniform spacing but with the same orientation as the wave-like features. The transitional morphology was observed in regions with ~0.2° misorientation. Notably, this morphology was only observed in regions of a substrate between regions of step flow and step bunching morphologies. The mean wavelength and amplitude of the wave-like features were found to be ~680 nm and ~1 nm, respectively. The spacing between bi-layer steps ranged from 50 nm to 120 nm with a mean spacing of 70 nm. Both the wave-like features and bi-layer steps were arrayed along the direction of the projection of the surface normal vector on the (0001) crystallographic plane. The RMS roughness in regions exhibiting the transitional microstructure was ~0.3 nm in $5 \times 5\ \mu m^2$ scan areas. The wave-like features in the transitional morphology are likely the result of an onset in step-step interactions between bi-layer steps that ultimately leads to the clustering of bi-layers observed in the step bunching morphology [32]. This theory is suggested by the transitional morphology exhibiting some characteristics of both the step flow and step bunching morphologies and both the upper limit of misorientations for the step flow microstructure and the lower limit of misorientations for the step bunching microstructure over lap at ~0.2°.

The layer-by-layer morphology is characterized by the same periodic arrays of bi-layer steps as the step flow morphology with the addition of two-dimensional nuclei on the bi-layer steps. These two-dimensional nuclei exhibit a triangular shape and are rotated 180°

from one another on alternating bi-layers steps. As with the step flow morphology, the spacing between bi-layer steps in the periodic array was found to be function of the misorientation of the crystal surface with the (0001) crystallographic plane and the direction of the step array was found to coincide with the direction of the projection of the surface normal vector on the (0001) crystallographic plane. The layer-by-layer morphology was observed in regions with misorientation values less than 0.07°. Bi-layer step spacing of 200 nm to 3700 nm and two-dimensional nuclei diameters of 30 nm to 300 nm where observed in regions that exhibit the layer-by-layer morphology. It is likely that the diameter of the largest nuclei partially resulted from the coalescence of multiple smaller nuclei as the mean spacing between nuclei centers was found to be 120 nm. The RMS roughness in regions exhibiting the layer-by-layer morphology was found to be ~0.1 nm in 5×5 μm^2 scan areas. The formation of two-dimensional nuclei implies a supersaturation of adatoms on the substrate surface during AlN deposition. This surface supersaturation is analogous to the gas phase supersaturation described in section 2.5 and represents the driving force to incorporate excess adatoms on the substrate surface and is a function of the surface diffusion length of adatoms, the flux of adatoms to the substrate surface from the gas phase, and the bi-layer step width [21]. The bi-layer step width dependence of surface supersaturation is due to the role of bi-layer steps as sinks for adatoms to be incorporated into the substrate. In particular, the two-dimensional nucleation in regions exhibiting the layer-by-layer morphology is likely the result of increased spacing between bi-layer steps relative to regions exhibiting the step flow morphology as regions of layer-by-layer and step flow morphologies have been observed in

regions immediately adjacent to one another on the same AlN substrate followed AlN deposition with a σ_{Al} of 4.2×10^4.

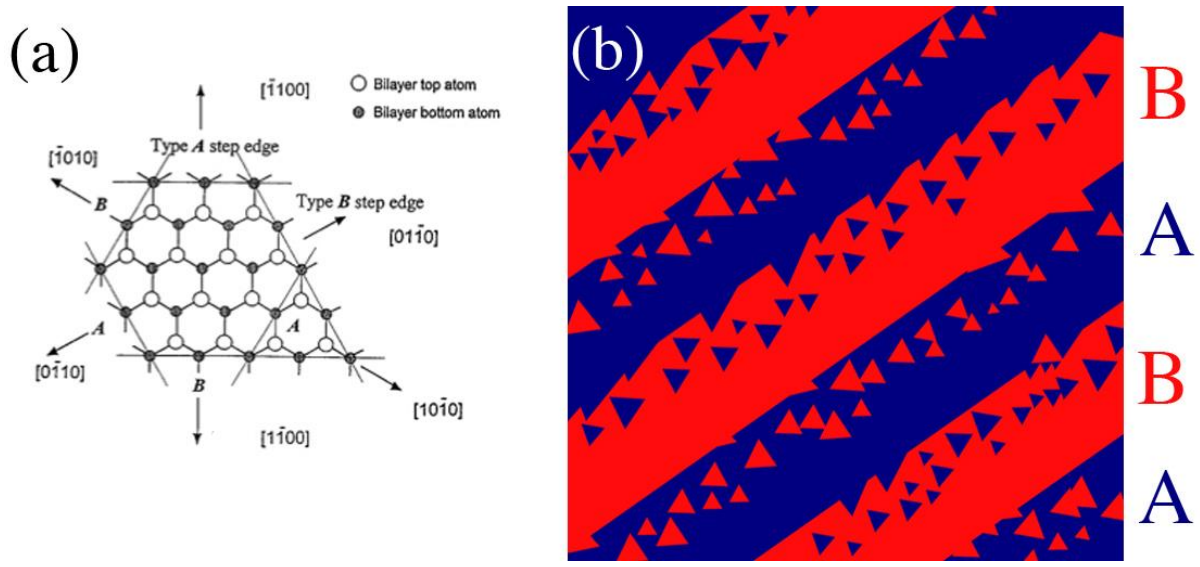

Figure 2-15: (a) Plan view schematic of the anisotropic bonding along the different <1-100> directions in a wurtzite bilayer. Reproduced from the work of Xie *et al.* [32]. (b) A pictorial overlay of Figure 2-13 (d) demonstrating how alternating bi-layers with 180° rotations could yield the observed morphology.

Xie *et al*. proposed a model to explain bi-layer islands in GaN films that exhibited similar geometry to the two-dimensional nuclei in the layer-by-layer morphology [32]. According to the model by Xie *et al.*, the differences in bonding along the <1-101> directions lead to differences in the step energy associated with [1-100] directions with a single bond and [10-10] directions with double bonds [32]. This effectively reduces the symmetry of each bi-layer to three-fold, and this three-fold symmetric system is rotated by 180° for alternating

bi-layers in an ABAB type packing order along the <0001> direction. Figure 2-15 (a) shows a schematic of for wurtzite bi-layers showing two difference types of bonding along <1-100> directions. Figure 2-15 (b) shows a pictorial representation of this ABAB packing order with 180° rotation of the triangular island on alternating bi-layer using the AFM topograph shown in Figure 2-13 (d) as a template.

2.7 Effects of Deposition Conditions on AlN Surface Morphology

The morphologies described in Section 2.6 represent only those present at the described deposition conditions and other morphologies have been observed when deposition is preformed at other conditions. Two major morphological differences to those already described are a transition from layer-by-layer growth to multilayer growth for regions with small misorientations and different step bunching behaviors for regions of large misorientations. The principle difference between the layer-by-layer growth and multilayer is the behavior of two-dimensional nucleation, and more specifically whether an addition nucleation occurs on a preexisting nuclei prior to the coalescence of the underlying layer determines the growth mode. This multilayer morphology was observed of AlN homoepitaxial films deposited with a S_{Al} of 1.4×10^{7}, and an AFM topograph of this morphology can be seen in Figure 2-16. A number of mound like features are present instead of the directional array of steps present in all of the previous described morphologies. As with the layer-by-layer morphology, triangular of two-dimensional nuclei are observed with the alternating 180° rotation between alternating bi-layers steps. The lateral dimensions of the triangular nuclei were between 30 nm and 500 nm and the largest of the nuclei were not

equiaxed. Circular or hexagonal nuclei of similar dimensions were also present but appeared more frequently as bi-layers lower in the mounds, suggesting that they are the result of coalescence and/or growth of smaller nuclei. The RMS roughness in regions exhibiting the multilayer morphology was found to ~0.1 nm in 5 µm x 5 µm, similar to the layer-by-layer morphology.

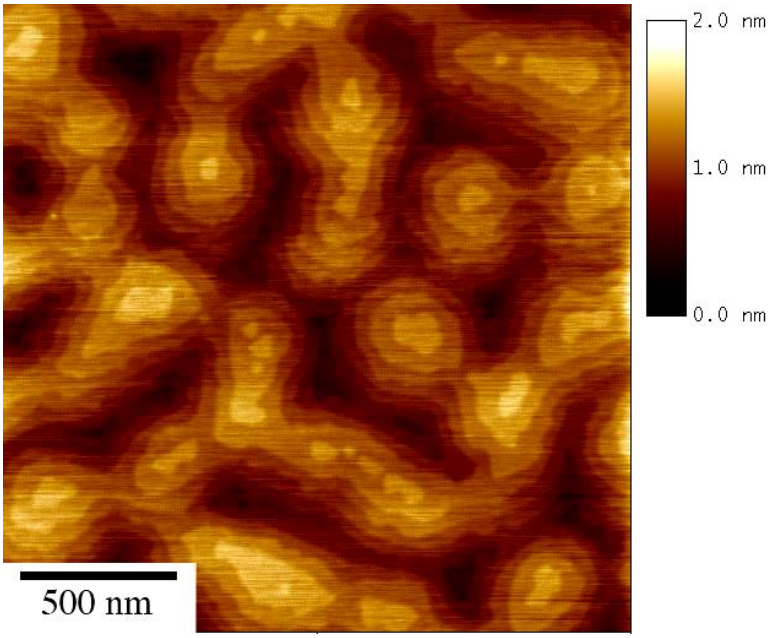

Figure 2-16: 2 µm x 2 µm AFM topograph of a 200 nm thick AlN homoepitaxial film deposited with an σ_{Al} of 1.4×10^{7} exhibiting the multilayer morphology.

There are a number of possible explanations for the transition from a layer-by-layer morphology to a multilayer morphology with increasing σ_{Al}. Stable islands are expected to be smaller due to more favorable bulk energy relative to surface energy. Diffusivity would be expect to be lower at lower temperatures so adatoms are less likely to diffuse to the edge of

an preexisting island. If a Schwoebel barrier exists to adatoms diffusing off of a preexisting island, there is less thermal energy to overcome the barrier and more adatoms would remain on the island [34].

The exact misorientation at which the transition from the step-flow to the multilayer morphology remains unknown as the irregular spacing of the terraces in the multilayer morphology prohibit the use of the $\tan(\alpha) = h/d$ relationship. It is likely that the upper misorientation limit for the multilayer morphology of AlN films deposited with a σ_{Al} of 1.4×10^7 is somewhat larger than 0.07°, the upper misorientation limit of layer-by-layer morphology of AlN films deposited with a σ_{Al} of 4.2×10^4, as the size of the critical nuclei is expected to be smaller.

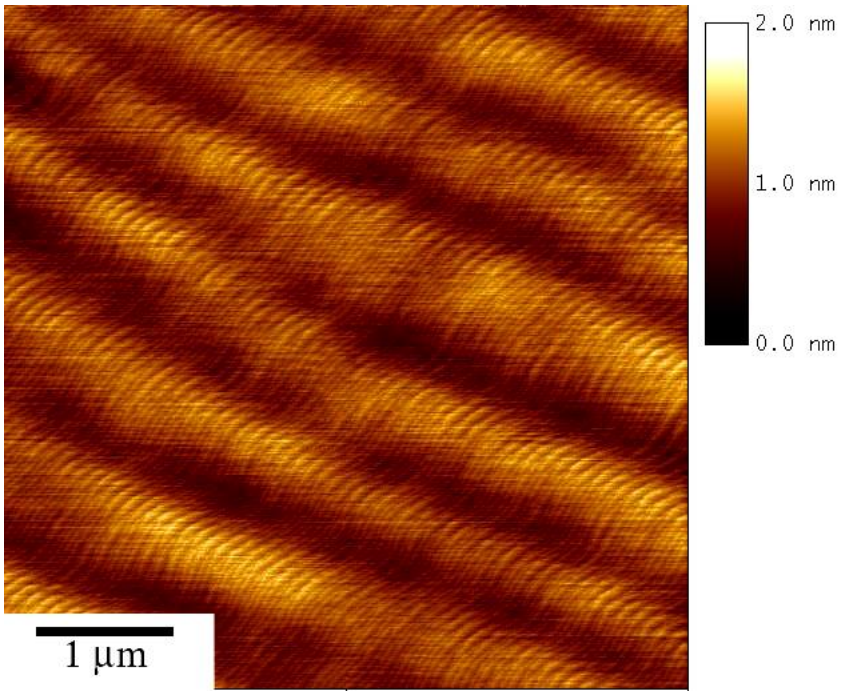

Figure 2-17: 5 x 5 µm^2 AFM topograph of a 1 µm thick AlN homoepitaxial film deposited with a σ_{Al} of 1.4×10^7 exhibiting the step flow morphology. The misorientation is ~0.3°.

2.8 Pitting and Misoriented Grains in AlN Homoepitaxial Films

Pitting and misoriented grains were two microstructural defects observed in the AlN homoepitaxial films in this study. These surface pits exhibited an inverted hexagonal pyramid morphology with sidewalls inclined at ~30° relative to the film surface normal. Pits observed in homoepitaxial films grown on substrates with misorientations larger than a few degrees show preferential elongation along the direction of the in-plane misorientation, strongly suggesting a crystallographic relationship between the surface of the film and sidewalls of the pits. This ~30° angle roughly corresponds to the inclination angle of the low index {10-11} planes to the (0001) plane of the AlN wurtzite lattice, similar to the so-called "V-defects" previously observed in GaN, InGaN, and AlGaN epilayers [35-37]. Transmission electron microscopy studies of GaN and InGaN have shown that many V-defects are generated at the intersection of threading dislocations with the film surface and are thought to be the result of crystalline faceting of the {10-11} planes during c-plane growth [35-37]. A schematic representation of typical V-defect structure reported in the literature is shown in Figure 2-18; the same figure shows also a representative AFM topograph of an 1 um AlN film deposited with an σ_{Al} of 1.4×10^7 on and (0001)-oriented AlN substrate with less than 1° misorientation.

In all homoepitaxial AlN films that exhibited pitting, the site density of hexagonal pits was highly non-uniform over the films' surface, varying from less than 10^4 cm^{-2} over most of the films' surface to as much as 10^7 cm^{-2} in some localized regions. The pit density depended on the microstructure of the underlying AlN substrate with the greatest pit density occurring in regions of the films corresponding to regions of the substrates containing low

angle grain boundaries, as revealed by defect-selective etching, which are known to consist of arrays of dislocations with a density greater than surrounding matrix [38]. The correspondence between regions with high hexagonal pit density and regions with low angle grain boundaries in our AlN films and substrates, respectively, suggests that the pits in the AlN films arise from a similar mechanism as the reported V-defects in the other nitrides. The fact that some pits were arranged in well-defined linear arrays also supports this assertion.

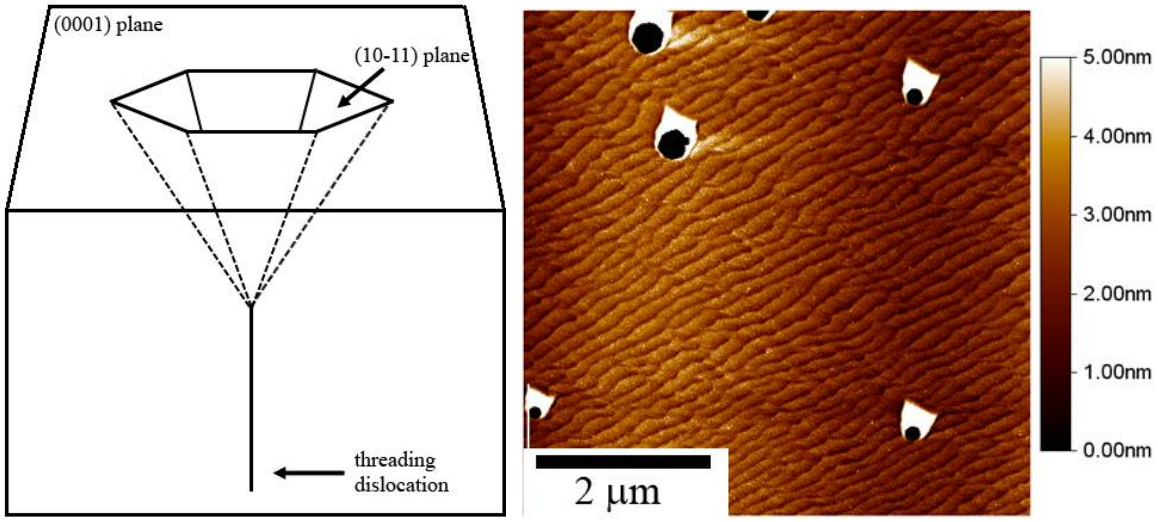

Figure 2-18: (a) Schematic of the hexagonal pit defects observed in the nitrides. The inverted hexagonal pyramid consist of {10-11} planes that intersect at a threading dislocation. (b) AFM topograph of a 1 μm thick AlN homoepitaxial film deposited with an σ_{Al} of 1.4×10^{7} on an (0001)-oriented AlN substrate with less that 1° misorientation. The white features are scan artifacts associated with large vertical scale changes. The pit density was 10^{7} cm^{-2}.

To further examine the nature of the hexagonal pits, cross-sectional TEM foils were prepared by site-selective focused ion beam milling. These foils were fabricated with a-plane

flats and were coated with carbon and platinum for masking during milling. Figure 2-19 shows a Z-contrast TEM micrograph where an apparently open core, threading dislocation is located at the base of a hexagonal pit with the inner facets of the pit forming the characteristic ~60° angle with one another, as expected for the {10-11} planes of the AlN wurtzite lattice and of the V-defects reported in other nitride systems. The mottled appear of the TEM micrograph is likely beam damage from the FIB sample preparation. Based on visibility conditions, the dislocation was identified as a mixed type dislocation.

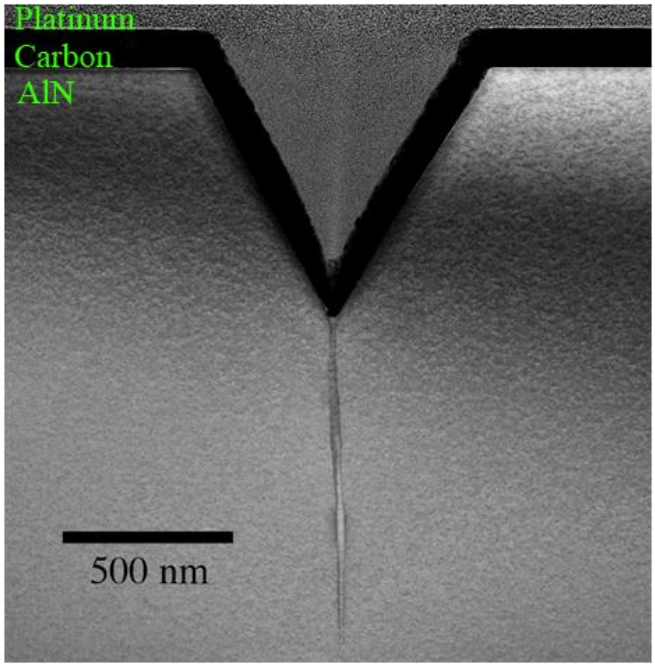

Figure 2-19: Cross-sectional Z-contrast TEM image of a hexagonal pit in a 3 μm thick AlN film deposited with an σ_{Al} of 1.4×10^{7} on an (0001)-oriented AlN substrate with less that 1° misorientation.

Frank studied dislocation pitting and developed a model for pit formation based on capillary equilibrium of a threading dislocation intersecting the free surface of a crystal to determine the critical conditions under which pitting would occur [39]. Frank proposed that the capillary equilibrium of the system depends on the energetic competition between the increase in surface energy due to the pit formation at the crystal surface and the reduction in strain energy of the crystal surrounding the dislocation that the pit would nucleate about. If specific facets are required for a stable pit to occur, then the pit formation can be suppressed by inhibiting the formation of those facets necessary to bound the pit. This can be achieved in practice by varying the terrace widths of the atomic steps of the crystal during deposition by modification of the process supersaturation. To this end, experiments were performed with a range of supersaturations to observe if this suppression of pitting could be achieved. It was found that pitting occur when AlN was deposited at the higher supersaturation conditions described in section 2.5, but pitting was absent when AlN was deposited at the lower supersaturation conditions. This demonstration suggests that surface pitting is an equilibrium phenomenon dependent on specific deposition conditions. Additionally, it was found that the dimensions of the pit features increased with increasing thickness of deposited AlN at the higher supersaturation conditions. Figure 2-20 shows a plot of the hexagonal pits widths as a function of AlN film thickness. The pit width was measured between opposing sidewalls of each pit at the intersection of the sidewall with the film surface and was found to increase at roughly 300 nm per 1000 nm of AlN film thickness.

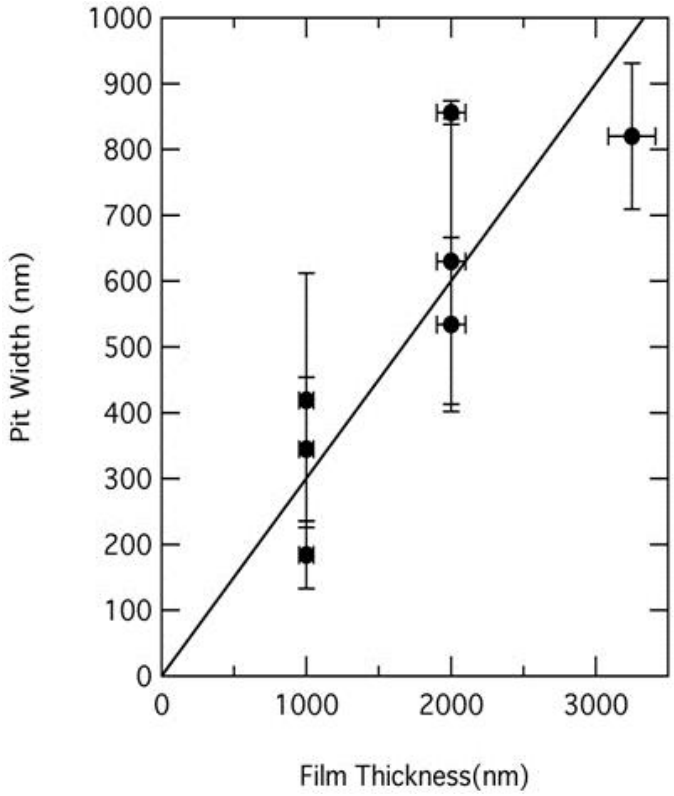

Figure 2-20: Pit width as a function of AlN film thickness for $\sigma_{Al} = 1.4\times10^{7}$.

Additional experiments were performed to test the equilibrium conditions for pit opening. As described above, it had been observed that the pit width increased as a function of film thickness. Thus, films of a given thickness grown under supersaturation conditions favorable for pit opening contained pits of a characteristic size, while thicker films contained larger pits. Based on this observation, 1 µm of homoepitaxial was AlN deposited with σ_{Al} of 4.2×10^{4}, conditions identified to exhibit no pitting, and then the process parameters were change and an additional 1 µm of AlN was deposited with σ_{Al} of 1.4×10^{7}, conditions identified to exhibit pitting. When the as-grown surface was examined, pits with dimensions characteristic of a 1 µm thick film were observed, indicating that while, the dislocations

threaded the entire film structure, open pits were only produced when the equilibrium conditions favored their formation. Figure 2-21 shows a schematic representation of these results.

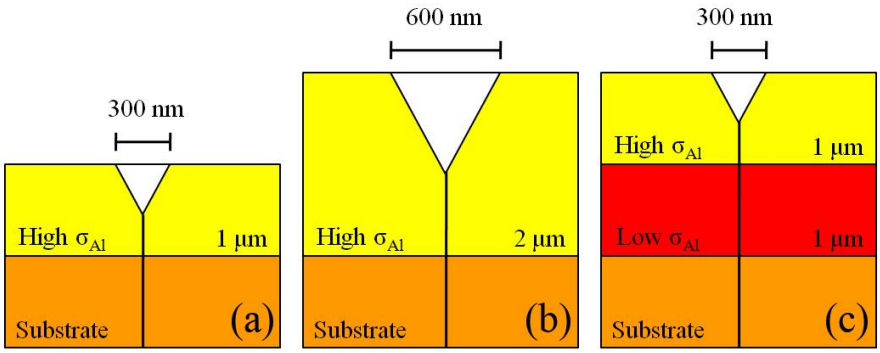

Figure 2-21: Schematic representation of the pitting behavior in homoepitaxial AlN deposited at different supersaturation conditions and with different thicknesses.

In general, for films grown at high superstaturation, pits formed with a width ~30% of the total film thickness (Figure 2-21 (a) and (b)). When a portion of the total film thickness was deposited at a lower supersaturation, the pit width only depended of the thickness of the film deposited at the higher supersaturation (Figure 2-21 (c)). In all cases a threading dislocation would be expected to advance through the entire film thickness.

Misoriented grains were another microstructural defect observed in the AlN homoepitaxial films. The misorented grains could roughly be catagorized as either polyhedral grains that appear to be socketed into a surrounding pit or as irregular stalagmite-like grains. The lateral dimensions of the polyhedral type grains were less than the AlN film thickness. In some cases, a portion of the polyhedral grain projects above the surface of the AlN film

while in other cases the polyhedra remain fully recessed inside of the surrounding pit such that no portion of the grain projects above the surface of the film. Both types of polyhedral type misoriented grains were found to in the same regions of films with approximately equal site densities. The stalagmite type misorented grains occurred with less site density than the polyhedral type grains and with lateral dimensions greater than the AlN film thickness. The vertical dimensions of the stalagmite type misorented grains were not readily measureable, but are presumably of the same order as the AlN film thickness in which they are found and were always projecting above the film surface.

As with the hexagonal pits, the density of misoriented grains was non-uniform across the AlN films with from less than 10^4 cm^{-2} over most of the films' surface to as much as 10^6 cm^{-2} in some localized regions correspond to a low angle grain boundary in the AlN substrate, suggesting that the misoriented grains were also associated with threading dislocations. Unlike the hexagonal pits, misoriented grains were observed in AlN films deposited with any of the supersaturation conditions used in this study, suggesting that the misoriented grains are operating with different criteria for nucleation than the hexagonal pits. Figure 2-22 shows a representative SEM micrograph of a 3 µm thick AlN film deposited with 1.4×10^7 on an AlN substrate with less than 1° misorientation. The SEM micrograph was taken of a region known to correspond to a low angle grain boundary in the AlN substrate. Hexagonal pits with site density of 10^7 cm^{-2} were observed in this region along with recessed and projecting polyhedral grains with a site density of 10^6 cm^{-2} and one stalagmite-like grain.

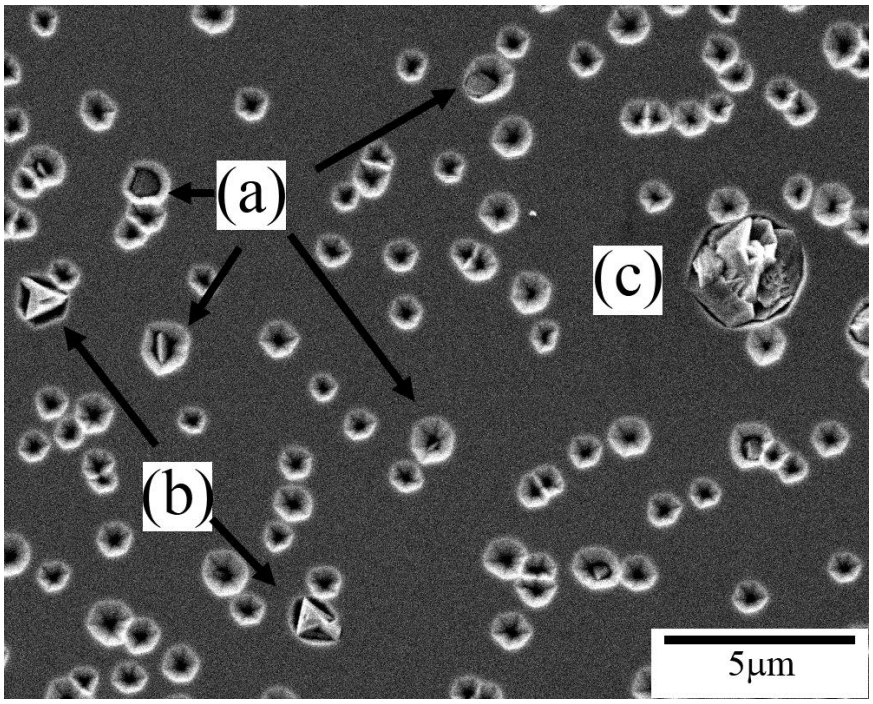

Figure 2-22: SEM micrograph of a 3 μm thick AlN film deposited with σ_{Al} 1.4×10^{7} on an AlN substrate with less than 1° misorientation. Hexagonal pits, (a) recessed and (b) projecting polyhedral grains, and a stalagmite-like grain can been seen.

Site-specific cross-sectional TEM samples of a 3 μm thick AlN film deposited with σ_{Al} of $1.4\text{x}10^{7}$ were prepared by FIB to further characterize the nature and cause of the misoriented grains. Figure 2-23 (a) shows a <01-10> bright field TEM micrograph with the entire misoriented grain and surrounding pit. The grain is not visible as it does not meet the

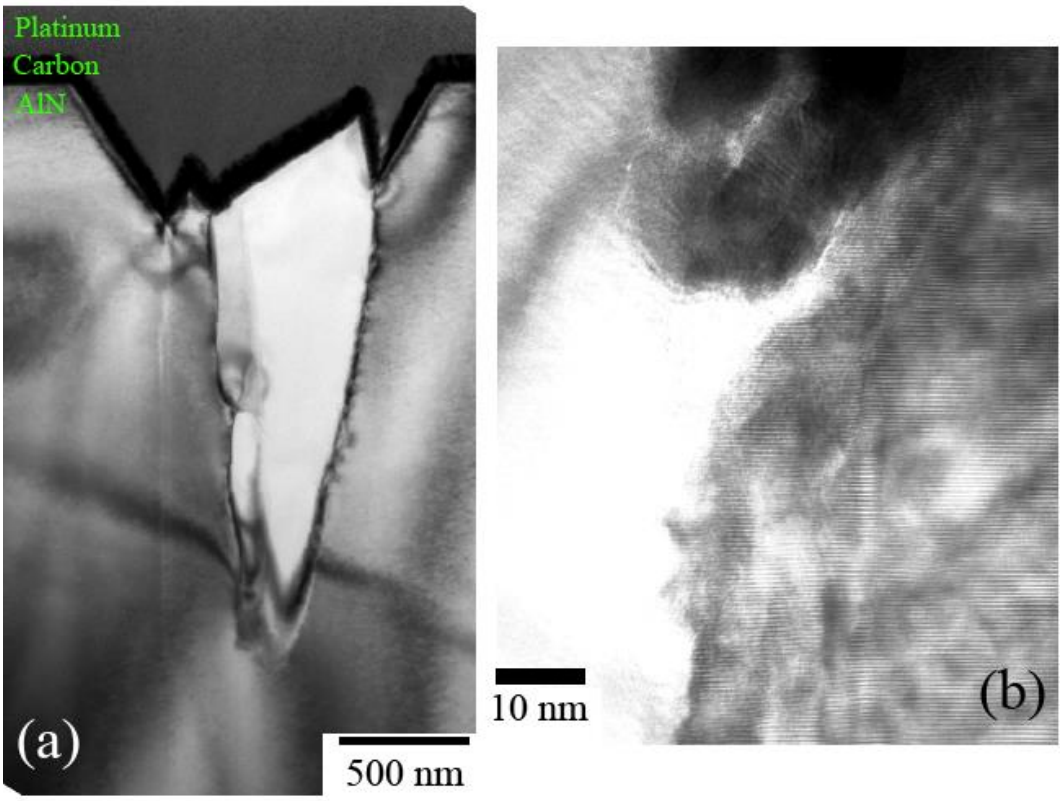

Figure 2-23: Cross-sectional TEM micrographs of a misoriented AlN grains in a 3 µm thick AlN film deposited with σ_{Al} of 1.4×10^{7}. (a) A lower magnification <01-10> bright field images showing the entirety of the misoriented grain and the surrounding pit. (b) A higher resolution phase contrast image of the base of the misoriented grain showing the network of threading dislocations.

Bragg condition at the zone-axis due the misorientation relative to the matrix. A separate threading dislocation or dislocations can also be seen to the left of the misoriented grain and appears to have formed a hexagonal pit, but the upper portion of the right sidewall of the pit is unformed due the proximity of the misoriented grain. Figure 2-23 (b) shows a high-resolution phase contrast image of the lowest portion of the misoriented grain where

numerous threading dislocations are clustered. Additional TEM studies located dislocations bounding the interfaces between the misorented grain and the matrix, but were unable to determine if these interface dislocations propagated from the threading dislocations or if there were introduced by the nucleation and grown of the misoriented grains. These results suggests that the primary difference between the formation of hexagonal pits and of misoriented grains is the number of threading dislocations or types of threading dislocations necessary for each defect to form with fewer threading dislocation present at hexagonal pits and a cluster of interacting threading dislocations for misoriented grains. This also presents one possible explanation for the variations in the forms of the misoriented grains, which can differ in volume by order of magnitude on the same film as there are presumably an innumerable combination of clustered dislocations.

2.9 Conclusions

The surface morphology and surface chemistry of MP and CMP (0001)-oriented AlN substrates following surface preparation were characterized and the implications for homoepitaxial deposition were discussed. MP substrates showed polishing damage while CMP substrates were atomically flat. Greater amounts of surface hydroxide were observed on MP substrates than on CMP substrates. Wet etching with sulfuric and phosphoric acid mixtures reduced the amount of surface hydroxide. The experimental behavior of hydroxides during high temperature ammonia annealing was found to be in agreement with a proposed thermodynamic model for nitridation. Though the amount and composition of hydroxides differed for MP and CMP substrates, ammonia annealing transformed both substrate surfaces

to AlN. However, MP substrates were found to roughen during annealing while CMP substrates were found to remain smooth. Aluminum supersaturation during epitaxial layer deposition was found to affect AlN nucleation. Epitaxial layers deposited on MP substrates were strained due to nucleation and coalescence of AlN grains on the mechanically damaged and roughened surfaces, and the strain state of such films was found to be a function of aluminum supersaturation. Successful AlN homoepitaxy was achieved by deposition on CMP substrates. The surfaces of AlN epitaxial layers on misoriented AlN substrates were found to take on four distinct morphologies, with each morphology occupying a finite range of misorientation values. Surface pitting and misoriented grains were observed in AlN epitaxial layers on AlN substrates. The density of these defects was non-uniform across samples with higher densities of defects in regions correspond to a low angle grain boundary in the AlN substrate.

2.10 References

1 G. A. Slack and T. F. McNelly, J. Cryst. Growth **34**, 263 (1976).

2 P. Bowen, J. G. Highfield, A. Mocellin, and T. A. Ring. J. Am. Ceram. Soc. **73**, 724 (1990).

3 H. M. Liao, R. N. Sodhi, and T. W. Coyle, J. Vac. Sci. Technol. A. **11**, 2681 (1993).

4 M. Sternitzke, J. Am. Ceram. Soc. **76**, 2289 (1993).

5 S. W. King, J. P. Barnak, M. D. Bremser, K. M. Tracy, C. Ronning, R. F. Davis, and R. J. Nemanich J. Appl. Phys. **84**, 5248 (1998).

6 L. M. Svedberg, K. C. Arndt, and M. J. Cima, J. Am. Ceram. Soc. **83**, 41 (2000).

7 J. Li, M. Nakamura, T. Shirai, K. Matsumaru. C. Ishizaki, and K. Ishizaki, J. Am. Ceram. Soc. **89**, 937 (2006).

8 R. Dalmau, R. Collazo, S. Mita, and Z. Sitar, J. Electron. Mater. **36**, 414 (2007).

9 H. Kawakami, K. Sakurai, K. Tsubouchi, and N. Mikoshiba, Jpn. J. Appl. Phys. **27**, L161 (1988).

10 A. Yamamoto, M. Tsujino, M. Ohkubo, and A. Hashimoto, J. Cryst. Growth **137**, 415 (1994).

11 K. Masu, Y. Nakamura, T. Yamazaki, T. Shibata, M. Takahashi, and K. Tsubouchi, Jpn. J. Appl. Phys. **34**, L760 (1995).

12 K. Uchida, A. Watanabe, F. Yano, M. Kouguchi, T. Tanaka, and S. Minagawa, J. Appl. Phys. **79**, 3487 (1996).

13 C. Heinlien, J. Grepstad, T. Berge, and H. Riechert, Appl. Phys. Lett. **71**, 341 (1997).

14 M. Yeadon, M. T. Marshall, F. Hamdani, S. Pekin, H. Morkoç, and J .M. Gibson, J. Appl. Phys. **83**, 2847 (1998).

15 C. Heinlein, J. Grepstad, S. Einfeldt, D. Hommel, T. Berge, and A. P. Grande, J. Appl. Phys. **83**, 6023 (1998).

16 Y. Cho, Y. Kim, E. R. Weber, S. Ruvimov, and Z. Liliental-Weber, J. Appl. Phys. **85**, 7909 (1999).

17 T. Hashimoto, Y. Terakoshi, M. Yuri, M. Ishida, O. Imafuji, T. Sugino, and K. Itoh, J. Appl. Phys. **86**, 3670 (1999).

18 M. Sumiya and S. Fuke, Appl. Surf. Sci. **244**, 269 (2005).

19 A. Koukitu, T. Taki, N. Takahashi, and H. Seki, J. Cryst. Growth **197**, 99 (1999).

20 A. Koukitu and Y. Kumagai, J. Phys.: Condens. Matter **13**, 6907 (2001).

21 W. K. Burton, N. Cabrera, and F. C. Frank, Philos. Trans. R. Soc. London Ser. A **243**, 300 (1951).

22 Z. G. Herro, D. Zhuang, R. Schlesser, R. Collazo, and Z. Sitar, J. Cryst. Growth **286**, 205 (2006).

23 D. Zhuang, R. Schlesser, and Z. Sitar, J. Cryst. Growth **287**, 372 (2006).

24 P. Lu, R. Collazo, R. F. Dalmau, G. Durkaya, N. Dietz, B. Raghothamachar, M. Dudley, and Z. Sitar, J. Cryst. Growth **312**, 58 (2009).

25 H. Helava, T. Chemekova, O. Avdeev, E. Mokhov, S. Nagalyuk, Y. Makarov, and M. Ramm, Phys. Status Solidi C **7**, 2115 (2010).

26 J. F. Moulder, W. F. Stickle, P. E. Sobol, and K. D. Bomben, Handbook of X-ray Photoelectron Spectroscopy (Eden Prairie, MN: Perkin-Elmer Corporation, 1982), p. 252.

27 M. A. G. Halliwell and S. J. Chua, J. Cryst Growth **192**, 456 (1998).

28 T. Tsuchida and H. Takahashi, J. Mater. Res. **9**, 2919 (1994).

29 C. D. Wagner, D. A. Zatko, and R. H. Raymond, Anal. Chem. **52**, 1445 (1980).

30 M. Dingne, P. Sautet, P. Raybaud, H. Toulhoat, and E. Artacho, J. Phys. Chem B **106**, 5155 (2002).

31 S. Mita, R. Collazo, A. Rice, R. F. Dalmau, and Z. Sitar, J. Appl. Phys. **104**, 013521 (2008).

32 M. H. Xie, S. M. Seutter, W. K. Zhu, L. X. Zheng, H. Wu, and S. Y. Tong, Phys. Rev. Lett. **82**, 2749 (1999).

33 V. A. Shchukin and D. Bimberg, Rev. Mod. Phys **71**, 1125 (1994).

34 R. L. Schwoebel and E. J. Shipsey, J. Appl. Phys. **37**, 3682 (1966).

35 P. –Y. Lin and Y Sermon Wu, Materials Chemistry and Physics, **80** 397 (2003).

36 H. K. Cho, J. Y. Lee, G. M. Yang, and C. S. Kim. Appl. Phys. Lett., **79** 215 (2001).

37 C. S. Ku, J. M. Peng, W. C. Ke, H. Y. Huang, N. E. Tang, W. K. Chen, W. H. Chen, and M. C. Lee. Appl. Phys. Lett., **85** 2818 (2004).

38 R. Dalmau, B. Moody, J. Xie, R. Collazo, and Z. Sitar, Phys. Status Solidi A, **208**, 1545 (2011).

39 F. C. Frank, Acta Cryst. **4**, 497 (1951).

CHAPTER 3: AlGaN Composition Control

3.1 Introduction

$Al_xGa_{1-x}N$ alloys with Al-mole fraction above 30% have been recognized as a crucial component for the development of deep UV optoelectronics. Several reports have suggested that kinetic barriers in the deposition of high Al-mole fraction $Al_xGa_{1-x}N$ limit the incorporation of Al into the growing film to a point that questions the thermodynamic stability of the alloy system [1, 2]. This is commonly evidenced by deviations from linearity in the functional relationship between the Al-mole fraction of the alloy and the group-III precursor input flows. Nevertheless, thermodynamic considerations indicate that all $Al_xGa_{1-x}N$ compositions are stable against phase separation and segregation [3]. MOCVD of $Al_xGa_{1-x}N$ alloys is further complicated by significant gas phase pre-reactions between the group-III precursors and NH_3, which is used at comparable flow-rates to the diluent gas. As such, precise control of $Al_xGa_{1-x}N$ alloy composition and deposition rate remains difficult, particularly at high deposition temperatures and pressures.

Xi *et al*. have proposed a model by which $Al_xGa_{1-x}N$ deposition can be described as a parallel processes of AlN and GaN deposition [4]. This model allows the prediction of the compositions and growth rates of $Al_xGa_{1-x}N$ layers to be made utilizing the linear combination of AlN and GaN growth rates for known group-III precursor input flows at the same deposition condition [4]. Mihopoulos *et al*. have proposed a model for $Al_xGa_{1-x}N$ deposition by conventional MOCVD that focuses principally on the depletion of available Al precursors by gas phase pre-reaction with NH_3 and the eventual formation of AlN particles large enough to be kept from the growth interface by thermophoretic forces [5]. Work by

Creighton *et al*. has confirmed the presence of particles of 10-100 nm diameter within the thermal boundary layer when group-III precursors and NH_3 are introduced at typical MOCVD temperatures and gas flow rates [6, 7].

In this article, we present the results of $Al_xGa_{1-x}N$ ($0 \leq x \leq 1$) deposition by MOCVD utilizing a range of group-III precursor and NH_3 flows. A linear relationship between the Al-mole fraction of $Al_xGa_{1-x}N$ layers and the group-III precursor flows is obtained with the use of a correction factor. It is demonstrated that the growth rate of $Al_xGa_{1-x}N$ layers is a linear combination of AlN and GaN growth rates under the same deposition conditions, as described by Xi *et al*. [4]. The dependencies of gas phase pre-reactions with group-III precursor and NH_3 concentrations are also explored.

3.2 Experimental Procedure

$Al_xGa_{1-x}N$/GaN heterostructures were deposited on c-plane sapphire substrates in a vertical, cold-walled, rf-heated, low-pressure MOCVD reactor with an open showerhead. The process total pressure was kept constant at 20 Torr throughout deposition. Triethylgallium (TEG), trimethylaluminum (TMA), and NH_3 were used as Ga, Al, and N precursors, respectively. Deposition was preceded by a substrate treatment consisting of H_2 annealing at 1100°C for 7 min and nitridation at 930°C for 4 min. A 10 nm thick AlN nucleation layer was deposited at 600°C and then annealed at the GaN and $Al_xGa_{1-x}N$ deposition temperature of 1050°C. After the annealing process, a 1.3 μm thick, Ga-polar GaN layer was deposited to serve as a pseudosubstrate for the subsequently deposited $Al_xGa_{1-x}N$ layer [8-11]. Heteroepitaxial deposition of $Al_xGa_{1-x}N$ on GaN was conducted with V/III ratios ranging

from 100-2000. The NH_3 mass flow was varied from 0.3-6.0 slm with N_2 diluent gas used to keep a constant 7.5 slm total mass flow during deposition. The TEG mass flow, f_{TEG}, was varied from 28-141 μmol/min and the TMA mass flow, f_{TMA}, was varied from 7-183 μmol/min assuming complete dissociation of TMA from the dimer to the monomer form upon entering the deposition chamber [5, 12]. The f_{TMA}/f_{TEG} ratio was varied from 0.05-3.32 to control the Al-mole fraction of $Al_xGa_{1-x}N$ layers.

$Al_xGa_{1-x}N$ layers were characterized by x-ray diffraction (XRD), which was performed using a Philips X'Pert materials research diffractometer with a Cu Kα x-ray source. To confirm reproducibility in film quality, on- and off-axis rocking curves were obtained in a double-axis configuration with a four-bounce Ge (220) crystal monochromator on the incident beam side and an open detector. Compositional analysis of $Al_xGa_{1-x}N$ layers was performed by the relative measurement of $Al_xGa_{1-x}N$ and GaN XRD peak positions utilizing symmetric scans of the (00.2) reflection and asymmetric scans of the (10.5) and (-10.5) reflections. The relative measurements provide strained $Al_xGa_{1-x}N$ lattice parameters that allow the determination of composition under the assumption of biaxial strain originating from lattice mismatch with the GaN pseudosubstrate [13]. Simulations utilizing the Philips X'Pert Epitaxy software package to solve the Takagi-Taupin equations were used to corroborate $Al_xGa_{1-x}N$ alloy compositions and film thicknesses. In situ optical transmission measurements by a pyrometer operating at 1.6 μm wavelength also allowed the approximation of film thicknesses and growth rates.

3.3 Results and Discussion

An increase in Al-mole fraction for $Al_xGa_{1-x}N$ layers was observed when the f_{TMA}/f_{TEG} ratio was increased during deposition. Figure 3-1 shows the variation of Al-mole fraction in $Al_xGa_{1-x}N$ layers deposited with a NH_3 partial pressure of 0.8 Torr as a function of the Al-mole fraction in the gas phase. The bowing, exhibited in Figure 3-1, indicates that the incorporation of Al differs from Ga under these particular deposition conditions (total flow, pressure, temperature, etc.) A linear relationship between the experimental Al-mole fraction

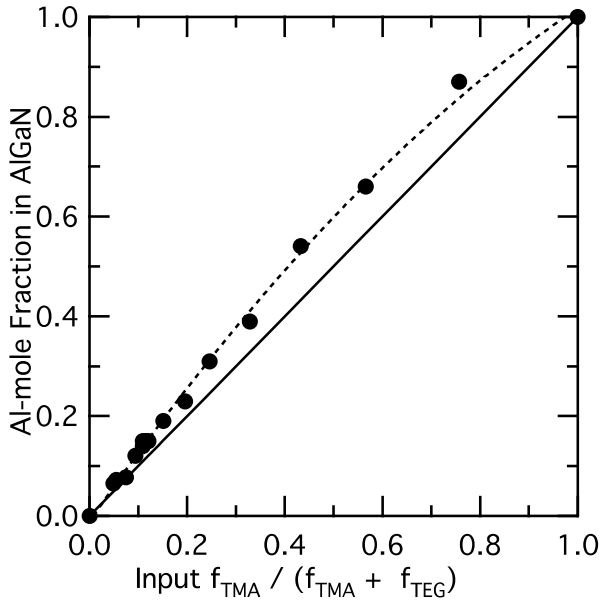

Figure 3-1: Variation of Al-mole fraction in $Al_xGa_{1-x}N$ layers deposited with a NH_3 partial pressure of 0.8 Torr as a function of input $f_{TMA}/(f_{TMA} + f_{TEG})$. The dashed line illustrates a polynomial fitting of the data. The solid line of slope 1 is included for reference to where the Al-mole fraction of the solid and gas phases would be equal.

of $Al_xGa_{1-x}N$ layers and the group-III precursor input flows was obtained if a correction factor, γ, was introduced such that:

$$x = \frac{\gamma f_{TMA}}{\gamma f_{TMA} + f_{TEG}} \tag{3-1}$$

This γ correction factor is a measure of the relative incorporation efficiency of each group-III precursor and is independent of the group-III precursor flows. γ was determined by regression analysis of Al-mole fraction in the deposited $Al_xGa_{1-x}N$ layers verses input $\frac{\gamma f_{TMA}}{\gamma f_{TMA} + f_{TEG}}$ data collected for a particular deposition condition. Figure 3-2 depicts the

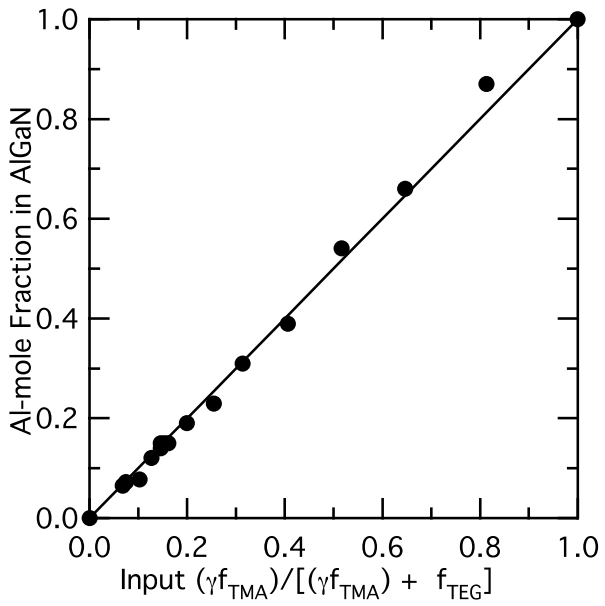

Figure 3-2: Variation of Al-mole fraction in $Al_xGa_{1-x}N$ layers deposited with a NH_3 partial pressure of 0.8 Torr as a function of input $\gamma f_{TMA}/(\gamma f_{TMA} + f_{TEG})$ with $\gamma = 1.4$. The line of slope 1 is included as a guide to the eye.

same series of $Al_xGa_{1-x}N$ growth runs used to construct Figure 3-1 but is plotted as the experimentally measured Al-mole fraction in the $Al_xGa_{1-x}N$ layer verses input $\gamma f_{TMA}/(\gamma f_{TMA} + f_{TEG})$ with $\gamma = 1.4$. This γ value of 1.4 signifies that the rate of Al incorporation into a growing $Al_xGa_{1-x}N$ film is 1.4 times greater than the rate of Ga incorporation with equal f_{TMA} and f_{TEG} under these deposition conditions.

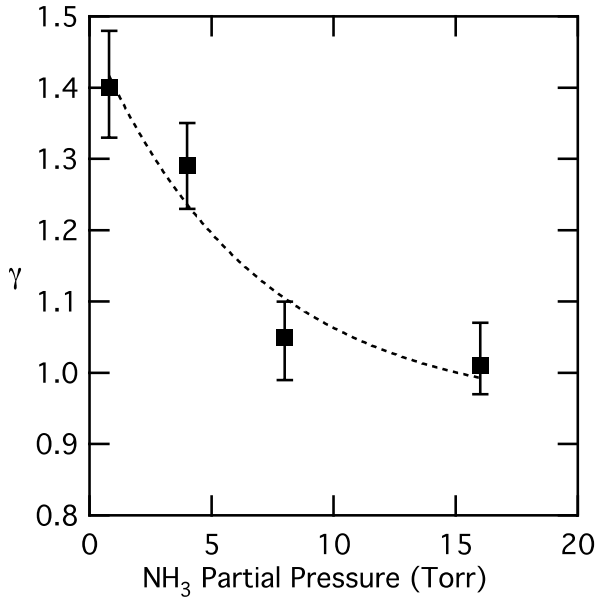

Figure 3-3: The change in relative incorporation ratios in $Al_xGa_{1-x}N$ layers deposited with varying NH_3 partial pressures. The dashed line illustrates an exponential fitting of the data.

However, as the apparent efficiency of incorporation depends on numerous factors such as the stability of each group-III precursor in the gas phase and at the growth interface, gas transport characteristics, as well as equipment calibration, the absolute value of relative incorporation ratios offer limited veracity. In contrast, changes in the relative incorporation ratios have significance as they indicate a variation in the behavior of each species with

respect to another as well as a referenced state. To determine the dependence of γ on deposition conditions, additional $Al_xGa_{1-x}N$ layers were deposited with NH_3 partial pressures of 4, 8, and 16 Torr with at least five different f_{TMA}/f_{TEG} ratios at each condition. The results of the γ factor dependence with NH_3 partial pressure during $Al_xGa_{1-x}N$ deposition are summarized in Figure 3. The exponential reduction in γ with increasing NH_3 partial pressure indicates that the incorporation efficiency of Al is reduced relative to Ga by increased NH_3 partial pressure.

Determination of γ for a particular deposition condition also allows the prediction of $Al_xGa_{1-x}N$ growth rates for combined group-III precursor flow rates under those conditions. The growth rate of $Al_xGa_{1-x}N$ films can be described as:

$$\frac{G}{G_o} = \frac{f_{III}}{f_{III_O}} , \tag{3-2}$$

where G is the $Al_xGa_{1-x}N$ growth rate and f_{III}, the effective total flow of group-III precursors, as given by: $f_{III} = \gamma f_{TMA} + f_{TEG}$. Equation 3-2 is referenced to a standard state (0) with a known growth rate and combined group-III precursor flow rate at the same deposition condition. Figure 3-4 shows the change in $Al_xGa_{1-x}N$ growth rate as a function of f_{III} for $Al_xGa_{1-x}N$ layers deposited with a NH_3 partial pressure of 0.8 Torr. Figure 3-4 demonstrates that the $Al_xGa_{1-x}N$ growth rate is the linear combination of the individual growth rates of AlN and GaN for a given group-III precursor flow under the particular deposition condition and is consistent with the findings of Xi *et al*. [4]. As GaN deposition under similar conditions in the growth reactor used for the currently presented experiments has been demonstrated to be

mass transfer limited with respect to f_{TEG}, it seems likely that the Al flux at the growth interface is also proportional to f_{TMA} for a particular deposition condition [8-11].

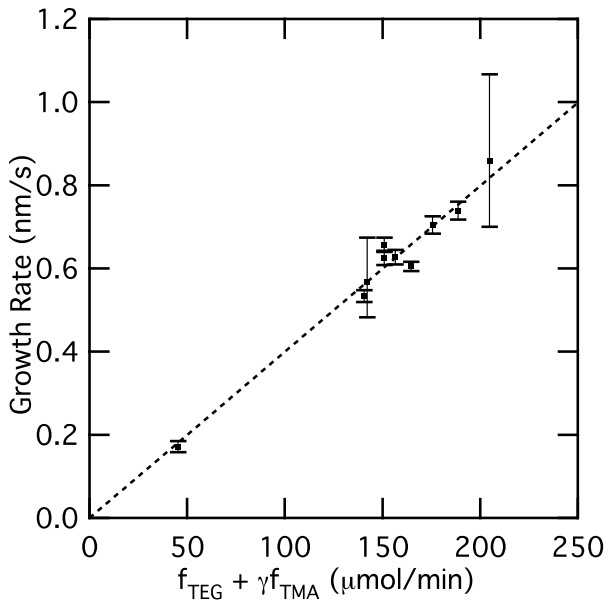

Figure 3-4: Growth rate of $Al_xGa_{1-x}N$ layers as a function of input f_{TMA} and f_{TEG} deposited with a NH_3 partial pressure of 0.8 Torr. γ = 1.4 under these conditions. The dashed line illustrates a linear fitting of the data.

Although the value of γ is determined by the incorporation efficiency of each group-III precursor, it is effectively a measure of the extent of gas phase pre-reactions between each group-III precursor and NH_3. This is suggested by its variability with reactor design and experimental conditions as can be concluded from a literature comparison; typical γ values for processes described in the literature range from 0.1-1 [2, 4, 5, 14-19]. As γ is independent of the group-III precursor flow rates for a particular set of deposition conditions, the rate controlling step for any pre-reaction involving either group-III precursor must necessarily be

of first order with respect to the precursor concentrations. Additionally, the change in γ with NH_3 partial pressure suggests that the gas phase pre-reaction of at least one group-III precursor must exhibit a non-zeroth order *[NH3]* dependency. As such, the rate limiting reaction for the effective reduction of each group-III precursor is expected to be of the form:

$$\frac{d[M]}{dt} = - k_M [M][NH_3]^{a_M}, \tag{3-3}$$

where *M* is either Al or Ga containing species, k_M is a rate constant, and α_M is the order of the reaction with respect to NH_3. Equation 3-3 can alternatively, and perhaps more intuitively, be written as a function of *z*, the distance gas has traveled beyond the position where group-III precursors have mixed with NH_3, assuming for simplicity gas flow through a vertical, cylindrical chamber with axially varying but radially uniform concentration profiles:

$$\frac{d[M]}{dz} = \frac{- k_M}{v} [M][NH_3]^{a_M}, \tag{3-4}$$

where *v* is the gas velocity and is given by $v = dz/dt$. Following separation of variables, integration, and the use of the boundary condition $[M] = [M]_o$ at $z = 0$, we have:

$$\ln \frac{[M]}{[M]_o} = - \int \frac{k_M}{v} [NH_3]^{a_M} dz. \tag{3-5}$$

Assuming for simplicity that k_M, *v*, *[NH3]*, and α_M are independent of position, Equation 3-5 may be rewritten as:

$$\frac{[M]}{[M]_o} = e^{\frac{-k_M}{v}[NH_3]^{a_M} z}. \quad (3\text{-}6)$$

This equation gives the fraction of input group-III precursor that remains unreacted for a given position. As γ decreases with increasing NH_3 partial pressure it can be concluded that either k_{Al} or α_{Al} or both are greater than k_{Ga} or α_{Ga}. Equations 3-4 and 3-5 have been left in a general case due to the fundamentally different behavior of the precursor gases depending on the proximity to the boundary layer. Within the boundary layer, v would be the mean molecular velocity during transport across the boundary layer. Far from the boundary layer, v would be the flow velocity of the gas mixture passing through the chamber. As gas phase pre-reactions between group-III precursors and NH_3 are expected in both regions, both cases could be reasonably assumed responsible for group-III precursor depletion without more accurate models of reaction pathways [20, 21].

Significant particle formation has been reported when group-III precursors and NH_3 are introduced into an MOCVD reactor operating at conditions similar to conventional $Al_xGa_{1-x}N$ deposition [6, 7]. A number of possible reaction pathways involving the formation of adducts have been proposed to explain the initiation of particle nucleation, but a complete understanding of intermediate steps is lacking [20, 21]. It is theorized that once particles have been formed, additional material is deposited onto the surfaces of such particles in a process analogous to conventional vapor phase epitaxy [6, 7]. Once a sufficient size is reached, thermophoresis prevents such particles from reaching the growth interface and contributing to the film deposition [5-7]. If the rate limiting process for group-III precursor depletion is the deposition by vapor phase epitaxy on suspended particles, both the first order dependency

with respect to the group-III precursor concentrations and the dependency on NH_3 concentration could be explained by the rate of collisions of precursor molecules with particles, as the impingement rate for a species is proportional to the concentration of that species. If N incorporation following collisions by NH_3 molecules is necessary for continued particle growth and continued group-III precursor depletion, it would be expected that α_{Al} = α_{Ga} = 1 as well. The effects of NH_3 depletion by such a mechanism would likely be negligible to the deposition of $Al_xGa_{1-x}N$ films, as NH_3 is typically supplied in excess on the order of 10^3 times the group-III precursor concentrations. Work by Creighton *et al.* demonstrated that 20-80% of all input TMA can be consumed by AlN particle formation under typical MOCVD conditions [6]. Under similar conditions, the fraction of TMG lost to GaN particles was estimated to be 10-50% of the TMA values [6]. While results for combined group-III precursor flows were not reported, it seems likely that the consumption of the individual group-III precursors by deposition on even a common form of particle would also be unequal.

As noted previously, γ values can be extracted from studies in the literature for Al-mole fraction experiments. This suggests that the phenomenon responsible for the non-linear relationship of Al-mole fraction in the gas phase and in the $Al_xGa_{1-x}N$ layers commonly reported is present in all conventional MOCVD systems and only varies in the severity in which it is observed between different systems configurations and experimental conditions. Figure 3-5 shows data series of Al-mole fraction in $Al_xGa_{1-x}N$ layers taken from the literature and from this work without (a) and with (b) the inclusion of the γ correction factor [4, 5, 17].

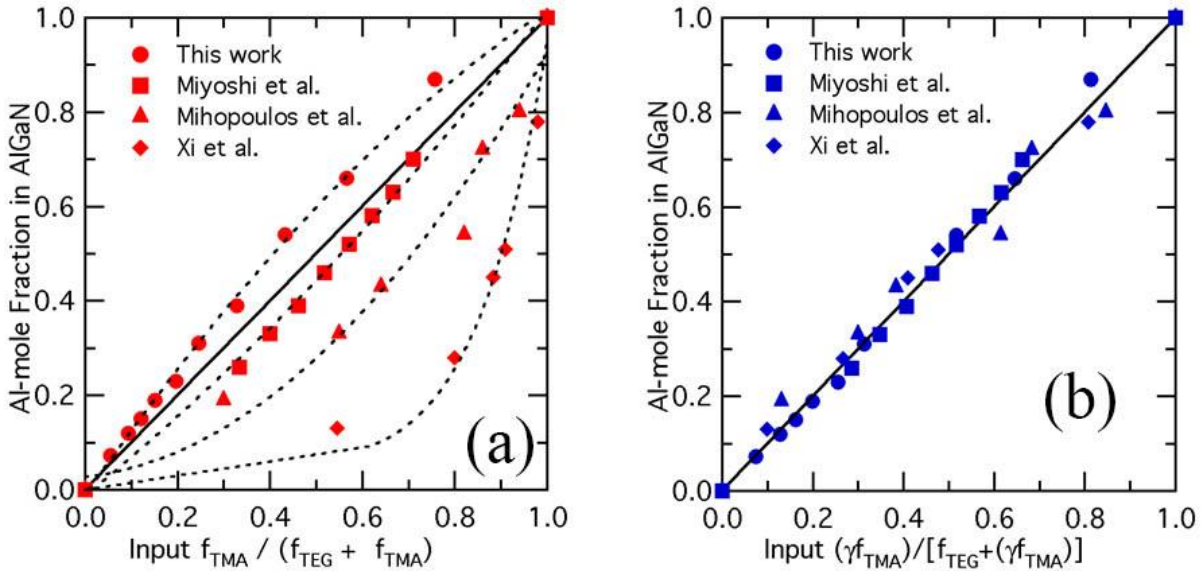

Figure 3-5: Variation of Al-mole fraction in $Al_xGa_{1-x}N$ layers taken from the literature and from this work without (a) and with (b) the inclusion of the γ correction factors.

3.4 Conclusions

A linear relationship between the experimental Al-mole fraction of $Al_xGa_{1-x}N$ layers and the group-III precursor flows was obtained if a correction factor γ was introduced such that $x = \frac{\gamma f_{TMA}}{\gamma f_{TMA} + f_{TEG}}$. The γ correction factor is independent of group-III precursor flows, but is dependent on other deposition parameters, such as NH_3 partial pressure. Although the value of γ is determined by the relative incorporation efficiency of each group-III precursor, it is thought to be a measure of the extent of gas phase pre-reactions between group-III precursors and NH_3. It is demonstrated that any such gas phase pre-reactions must necessarily be of first order with respect to the group-III precursor concentrations. The Al-mole fraction of $Al_xGa_{1-x}N$ layers was found to decrease for a given f_{TMA}/f_{TEG} ratio when the

flow of NH_3 was increased. The value of γ for these experiments decreased from 1.4 to 1.0 when the NH_3 partial pressure was increased from 0.8 to 16.0 Torr during $Al_xGa_{1-x}N$ deposition. The growth rate of $Al_xGa_{1-x}N$ layers was found to be a linear combination of the independent AlN and GaN growth rates when equivalent f_{TMA} and f_{TEG} were utilized under the same deposition conditions.

3.5 References

1 D. C. Lu, S. Duan, J. Crystal Growth 208 (2000) 73.

2 D.W. Song, H.J. Kim, Y.S. Jeon, E. Yoon, J. Crystal Growth 298 (2007) 367.

3 A. Koukitu, H Seki, Jpn. J. Appl. Phys. 35 (1996) L1638.

4 Y.A. Xi, K.X. Chen, F.W. Mont, J.K. Kim, W. Lee, E.F. Schubert, W. Liu, X. Li, J.A. Smart, Appl. Phys. Lett. 90 (2007) 051104.

5 T.G. Mihopoulos. V. Gupta, K.F. Jensen, J. Crystal Growth 195 (1998) 733.

6 J.R. Creighton, W.G. Breiland, M.E. Coltrin, R.P. Pawlowski, Appl. Phys. Lett. 81 (2002) 2626.

7 J.R. Creighton, G.T. Wang, W.G. Breiland, M.E. Coltrin, J. Crystal Growth 261 (2004) 204.

8 R. Collazo, S. Mita, A. Aleksov, R. Schlesser, Z. Sitar, J. Crystal Growth 287 (2006) 586.

9 A. Aleksov, R. Collazo, S. Mita, R. Schlesser, Z. Sitar, Appl. Phys. Lett. 89 (2006) 052117.

10 S. Mita, R. Collazo, R.F. Dalmau, Z. Sitar, phys. stat. sol. (c) 4 (2007) 2260.

11 S. Mita, R. Collazo, A. Rice, R.F. Dalmau, Z. Sitar, J. Appl. Phys. 104 (2008) 013521.

12 W.G. Breiland, M.E. Coltrin, J.R. Creighton, H.Q. Hou, H.K. Moffat, J.Y. Tsao, Mater. Sci. Reports R24 (1999) 241.

13 M. Schuster, P.O. Gervais, B. Jobst, W. Hosler, R. Averbeck, H. Riechert. A. Iberl, R. Stommer, J. Phys. D: Appl. Phys. 32 (1999) A56.

14 Y. Koide, H. Itah, N. Sawaki, I. Akasaki, M. Hashimoto, J. Electrochem. Soc. 133 (1986) 1956.

15 S. Ruffenach-Clur, O. Briot, J.L. Rouviere, B. Gil, R.L. Aulombard, Mater. Sci. Eng. B B50 (1997) 219.

16 S.C. Choi, J.H. Kim, J.Y. Choi, K.J. Lee, K.Y. Lim, G.M. Yang, J. Appl. Phys. 87 (2000) 172.

17 M. Miyoshi, M. Sakai, H. Ishikawa, T. Egawa, T. Jimbo, M. Tanaka, O. Oda, J. Crystal Growth 272 (2004) 293.

18 C. Touzi, F. Omnes, B. El Jani, P. Gibart, J. Crystal Growth 279 (2005) 31.

19 D.B. Li, M. Aoki, T. Katsumo, H. Miyake, K. Hiramatsu, T. Shibata, J. Crystal Growth 298 (2007) 372.

20 J.R. Creighton, G.T. Wang, J. Phys. Chem. A 109 (2005) 10554.

21 G.T. Wang, J.R. Creighton, J. Phys. Chem. A 110 (2006) 1094.

CHAPTER 4: Conclusions and Future Work

This dissertation has focused on III-nitride semiconductors composed of aluminum and gallium bonded with nitrogen. These nitrides are important because of characteristics they possess such as bandgaps that make photo-detectors, LEDs, and lasers possible, and also large breakdown fields and high electron mobilities that allow for radio-frequency operation and high-power electrical devices. To achieve their potential, it is necessary to address challenges in III-nitrides. One of these challenges is that little is known about the use of native substrates and the defect behavior in homoepitaxial films. Another challenge is that there are issues with non-ideality in incorporating Al and Ga into thin films relative to input Al and Ga concentrations during deposition. This dissertation addresses these challenges by developing a method for composition control in AlGaN thin films and surface morphology and growth mode control in homoepitaxial AlN thin films.

4.1 Overview of Research Findings

The research reported in chapter two focused on the usage of single crystalline AlN substrates for homoepitaxial growth of AlN thin films by metalorganic chemical vapor deposition. The surface morphology and surface chemistry of AlN substrates were characterized and the implications for homoepitaxial deposition were discussed. A thermodynamic model for nitridation of aluminum oxide by ammonia at high temperature was proposed and experimental data corroborated this model. AlN homoepitaxy was achieved by the growth on AlN substrates and was verified by HRXRD, TEM, and AFM characterization. Sufficiently large AlN substrate miscuts were found to produce macro-steps

for homoepitaxial AlN thin films. Increasing Al supersaturation during AlN thin film deposition increased the angle of miscut at which macro-steps would form. Threading dislocations from AlN substrates were found to produce hexagonal pits and misoriented grains in AlN thin films. Decreasing Al supersaturation during AlN thin film deposition suppressed the formation of such pits and misoriented grains, but subsequent AlN thin film deposition with higher Al supersaturation was found to produce such pits and misoriented grains as if the prior low Al supersaturation layer were absent.

In Chapter 3, a model of AlGaN composition control was developed and demonstrated. It was determined that the parasitic reaction was a first-order kinetic reaction. Because of the first-order behavior, a correction gamma is independent of the Al and Ga precursor concentrations. However, other variables, such as the ammonia concentration do affect gamma. And in the case of ammonia, increasing those concentrations decreases gamma. We found that nearly all reported AlGaN composition studies for various reactors could be linearized with an appropriate gamma factor. This suggested that the gamma was a tooling factor that depends on the system and deposition conditions.

4.2 Future Research

During the research for this dissertation, several further challenges where identified and need to be addressed in future research. One is that the miscut required to prevent macro-step formation during AlN homoepitaxy is extremely small for some deposition conditions. This challenge can be somewhat mitigated by using higher supersaturation during AlN growth, which increases the miscut at which macro-steps will form.

Threading dislocations from AlN substrates form pits and misoriented grains during deposition of AlN homoepitaxy under some deposition conditions. Low supersaturation can prevent pit and misoriented grain formation. No method is known to prevent dislocations following the growth interface. AlGaN films cause dislocation to split and create additional defects.

The orientation of the surface partially determines the composition of an AlGaN film. AlGaN films deposited on stepped surfaces show bi-modal compositions, which vary with the two growth faces. This results in AlGan films with macro-steps having interleaved bands of different AlGaN compositions. However, even AlGaN films on surfaces without macro-steps will have different compositions with different miscuts.

Lattice mismatch between AlN and GaN is sufficiently large that significant amounts of strain are typically present between layers of AlGaN and either end member or even layers of other AlGaN compositions. In the samples produced for use in this dissertation, a variety of strain states were observed. These included fully coherent films and partially relaxed AlGaN films on AlN and AlGaN. It likely that AlGaN films under compressive strain can exhibit non-catastrophic relaxation mechanisms, but this is not the case with tensile strain.